NASA Technical Memorandum 101557

A CELL-VERTEX MULTIGRID METHOD FOR THE NAVIER-STOKES EQUATIONS

R. Radespiel

JANUARY 1989

National Aeronautics and Space Administration

Langley Research Center
Hampton, Virginia 23665

Summary

A cell-vertex scheme for the Navier-Stokes equations, which is based on central difference approximations and Runge-Kutta time stepping, is described. Using local time stepping, implicit residual smoothing, a multigrid method, and carefully controlled artificial dissipative terms, very good convergence rates are obtained for a wide range of two- and three-dimensional flows over airfoils and wings. The accuracy of the code is examined by grid refinement studies and comparison with experimental data. For an accurate prediction of turbulent flows with strong separations, a modified version of the nonequilibrium turbulence model of Johnson and King is introduced, which is well suited for an implementation into three-dimensional Navier-Stokes codes. It is shown that the solutions for three-dimensional flows with strong separations can be dramatically improved, when a nonequilibrium model of turbulence is used.

Introduction

In recent years, considerable advancement has been achieved in the numerical solution of the Euler and Navier-Stokes Equations. Nevertheless, existing computer codes for the solution of the three-dimensional Navier-Stokes equations require large computing times. In order to make Navier-Stokes solutions useful in the flight vehicle design process, substantial improvements in efficiency and accuracy of the algorithms have to be made.

Finite-volume methods based on explicit Runge-Kutta time stepping schemes have been shown to be very efficient in the solution of the Euler equations governing inviscid flows [1,2]. They are in widespread use now. More recently, they have been extended for a solution of the mass-averaged Navier-Stokes equations. The convergence of the basic scheme to the desired steady state solution, however, slows down considerably because of the time step limitation associated with the small mesh cells which are necessary to resolve the thin shear layers. This drawback of the explicit scheme can be overcome by applying several acceleration techniques, namely local time stepping, implicit residual averaging and a multigrid algorithm. Successful applications of these techniques have been reported in [3,4] for two-dimensional flows and there has been a partial success in three dimensions also [5].

In the present work a recently developed efficient and robust finite-volume multigrid scheme for the two- and three-dimensional Navier-Stokes equation is presented. The scheme employs a cell-vertex discretization rather than the usual cell-centered discretization because an analysis of the discretization errors indicates lower errors for meshes with high stretching or discontinuities in slope. The accuracy of the treatment of the far-field boundary is improved by representing the lifting surface by a vortex and using the induced flow field to determine the free-stream conditions. As the scheme is based on central differencing, an artificial viscosity model is used, which is particularly designed for high aspect-ratio cells. The boundary treatment of the dissipative terms, which is important for an accurate prediction of the skin friction, is discussed. A multistage Runge-Kutta time-stepping algorithm is used to advance the solution in time. The acceleration techniques, which are applied to obtain faster

convergence, are discussed. For an accurate prediction of turbulent flows with strong separations, a modified version of the nonequilibrium turbulence model of Johnson and King [6] is introduced, which is well suited for an implementation into three-dimensional Navier-Stokes codes.

Numerical results for subsonic, transonic and supersonic flows around airfoils and finite span wings are given. The accuracy and the convergence behavior of the scheme are investigated by varying the grid density and the coefficient of the artificial dissipation. The influence of the turbulence model on the numerical results is shown for several flow cases. It is demonstrated that the solutions converge very rapidly to the steady state. Typically, engineering accuracy is obtained within 40 multigrid cycles for high Reynolds number transonic airfoil flows on a 321x65 mesh. For finite-span wings, converged solutions are obtained within 50-80 iterations on a mesh with 288x65x49 points.

Symbols

a	half span
c	speed of sound
c_f	skin-friction coefficient
c_p	pressure coefficient
C_D	drag coefficient
C_L	lift coefficient
CFL	Courant number of time stepping scheme
d	Distance from the wall
E	total internal energy
$\vec{i}_x, \vec{i}_y, \vec{i}_z$	unit vectors of Cartesian coordinate system
$K^{(2)}$	coefficient of the second difference dissipation
$K^{(4)}$	coefficient of the fourth difference dissipation
M	Mach number
$\vec{n}$	unit vector of outer normal
p	pressure
Pr	Prandtl number
$\vec{S}_\xi, \vec{S}_\eta, \vec{S}_\zeta$	cell face vectors in the ξ-, η-, and ζ- directions
t	time
T	temperature
u,v,w	Cartesian velocity components
V	volume
$\vec{W}$	vector of conserved quantities = $(\rho\ \rho u\ \rho v\ \rho w\ \rho E)^T$
x,y,z	Cartesian coordinates
α	angle of attack
γ	ratio of specific heats, intermittency factor

δ	central difference operator, boundary layer thickness
ε_ξ, ε_η, ε_ζ	coefficients of implicit smoothing according to (26)
κ	v. Karman's constant = 0.4
λ_ξ, λ_η, λ_ζ	spectral radii of the Jacobian matrices associated with the ξ-, η-, ζ-directions
μ	viscosity according to (4)
ρ	density
σ	nonequilibrium factor in J.-K.-mod. turbulence model
τ	shear stress
ω	exponent in (12) and (27)
Ω	magnitude of vorticity
ξ, η, ζ	curvilinear coordinates

Subscripts

i,j,k	discrete quantity
m	location of maximum of function g, equation (36), across boundary layer
max	location of maximum of function F, equation (34), across boundary layer
t	turbulent
w	value at the wall
∞	value infinitely far away from the aerodynamic surface

Governing Equations

The integral form of the mass-averaged Navier-Stokes equations using nondimensional variables can be written as

$$\frac{\partial}{\partial t}\iiint_V \vec{W}\, dV + \iint_{\partial V} \overline{F}\,\vec{n}\, dS = 0 \tag{1}$$

where

$$\vec{W} = (\rho\ \rho u\ \rho v\ \rho w\ \rho E)^T .$$

is the vector of conserved quantities with ρ, u, v, w, E denoting the density, the Cartesian velocity components and the specific total internal energy. The quantity V denotes an arbitrary control volume with the boundary ∂V and the outer normal $\vec{n}$. The flux tensor $\overline{F}$ may be divided into its convective part $\overline{F}_c$ and its viscous part $\overline{F}_v$ as

$$\overline{F} = \overline{F}_c - \overline{F}_v$$

$$\overline{F}_c = \begin{bmatrix} \rho u\,\vec{i}_x & + \rho v\,\vec{i}_y & + \rho w\,\vec{i}_z \\ (\rho u^2+p)\vec{i}_x & + \rho uv\,\vec{i}_y & + \rho uw\,\vec{i}_z \\ \rho uv\,\vec{i}_x & + (\rho v^2+p)\vec{i}_y & + \rho vw\,\vec{i}_z \\ \rho uw\,\vec{i}_x & + \rho vw\,\vec{i}_y & + (\rho w^2+p)\vec{i}_z \\ (\rho uE+up)\vec{i}_x & + (\rho vE+vp)\vec{i}_y & + (\rho wE+wp)\vec{i}_z \end{bmatrix}$$

$$\overline{F}_v = \begin{bmatrix} 0 & & \\ \sigma_{xx}\vec{i}_x & + \sigma_{xy}\vec{i}_y & + \sigma_{xz}\vec{i}_z \\ \sigma_{yx}\vec{i}_x & + \sigma_{yy}\vec{i}_y & + \sigma_{yz}\vec{i}_z \\ \sigma_{zx}\vec{i}_x & + \sigma_{zy}\vec{i}_y & + \sigma_{zz}\vec{i}_z \\ (u\sigma_{xx}+v\sigma_{xy}+w\sigma_{xz}-q_x)\vec{i}_x & +(u\sigma_{yx}+v\sigma_{yy}+w\sigma_{yz}-q_y)\vec{i}_y & +(u\sigma_{zx}+v\sigma_{zy}+w\sigma_{zz}-q_z)\vec{i}_z \end{bmatrix}$$

The equation of state for an ideal gas is used to calculate the pressure, p, and the temperature, T. That is,

$$p = (\gamma-1)\rho(E - (u^2+v^2)/2) , \quad T = p/\rho , \tag{2}$$

where γ denotes the ratio of specific heats. The elements of the shear-stress tensor and the heat-flux vector are given by the constitutive equations for a Newtonian fluid as follows:

$$\begin{aligned} \sigma_{xx} &= 2\mu u_x - 2/3\mu(u_x+v_y+w_z) \\ \sigma_{yy} &= 2\mu v_y - 2/3\mu(u_x+v_y+x_z) \\ \sigma_{zz} &= 2\mu v_z - 2/3\mu(u_x+v_y+x_z) \\ \sigma_{xy} &= \sigma_{yx} = \mu(u_y+v_x) \\ \sigma_{xz} &= \sigma_{zx} = \mu(u_z+w_x) \\ \sigma_{yz} &= \sigma_{zy} = \mu(v_z+w_y) \end{aligned} \tag{3}$$

$$q_x = -k\partial T/\partial x, \quad q_y = -k\partial T/\partial y, \quad q_z = -k\partial T/\partial z .$$

The nondimensional viscosity, μ, is assumed to follow an empirical power law

$$\mu = \frac{\gamma^{1/2} M_\infty}{Re_\infty} (T/T_\infty)^{0.75} \tag{4}$$

and the heat conductivity is

$$k = \frac{\gamma}{\gamma-1}\frac{\mu}{Pr} . \tag{5}$$

For turbulent flows, the laminar viscosity, μ, is replaced by $\mu+\mu_t$ and μ/Pr is replaced by $\mu/Pr+\mu_t/Pr_t$, where the eddy viscosity, μ_t, and the turbulent Prandtl number, Pr_t, are provided by a turbulence model. The turbulence models used in the present work are described in a subsequent paragraph.

Spatial Discretization

The discretization of (1) follows the method of lines, i.e. discretization in space and time are done separately. The domain around the aerodynamic body is partitioned with hexahedrons. The discrete values of the flow quantities are located at the vertices of the mesh

cells. The eight cells surrounding a vertex form a super cell as shown in Fig. 1. The integral equation (1) is approximated by the spatial discretization yielding

$$\frac{d}{dt}\vec{W}_{i,j,k} = \frac{1}{V_{i,j,k}}\left[\vec{Q}_{c\,i,j,k} + \vec{Q}_{v\,i,j,k} + \vec{D}_{i,j,k}\right]. \tag{6}$$

In the following, the net inflow of mass, momentum and energy associated with the convective terms $\vec{Q}_{c\,i,j,k}$, the viscous terms $\vec{Q}_{v\,i,j,k}$ and the artificial dissipative terms $\vec{D}_{i,j,k}$ are discussed. For this purpose the super cell around the point (i,j,k) for the simplified case of a plane mesh is shown in Fig. 2.

The surface integral of (1) is evaluated for each component cell using an arithmetic average of the flux quantities at the vertices to determine the values on each of the boundary segments. Then the resultant convective inflow of mass, momentum and energy associated with point (i,j,k) is computed by summing the contributions of the component cells. According to [7], the scheme is at least first-order accurate, if two conditions are satisfied. (1) The distribution of the normal vector over each surface segment has to be smooth, that is, if the grid is refined, the four grid points defining a segment tend to lie within a plane. (2) The shape of each surface segment has to approach a parallelogram with grid refinement. Note, that these conditions still allow discontinuities in the slope of the grid lines and discontinuities in the rate of grid stretching. On completely smooth meshes, the discretization is second-order accurate.

Next, the viscous fluxes required to determine the solution at the point (i,j,k) are approximated using the auxiliary cell with the dashed boundary shown in Fig. 2. The viscous fluxes contain first derivatives of the flow variables, which are computed using a local transformation from Cartesian coordinates to the curvilinear coordinates ξ,η,ζ, i. e.

$$\phi_x = \frac{\partial\phi}{\partial\xi}\frac{\partial\xi}{\partial x} + \frac{\partial\phi}{\partial\eta}\frac{\partial\eta}{\partial x} + \frac{\partial\phi}{\partial\zeta}\frac{\partial\zeta}{\partial x} \tag{7}$$

The derivatives ϕ_ξ, ϕ_η and ϕ_ζ are approximated using finite differences, whereas the cell face vectors $\vec{S}_\xi$, $\vec{S}_\eta$, $\vec{S}_\zeta$, which are written as

$$\vec{S}_\xi = (S_{\xi x}\ S_{\xi y}\ S_{\xi z})^T$$
$$\vec{S}_\eta = (S_{\eta x}\ S_{\eta y}\ S_{\eta z})^T$$
$$\vec{S}_\zeta = (S_{\zeta x}\ S_{\zeta y}\ S_{\zeta z})^T,$$

and the volume V are used to compute metric derivatives. If ϕ_x is to be approximated at (i+1/2,j,k) we obtain

$$(\phi_x)_{i+1/2,j,k} = \frac{\delta_\xi\phi_{i+1/2,j,k}\ S_{\xi x_{i+1/2,j,k}} + \delta_\eta\phi_{i+1/2,j,k}\ S_{\eta x_{i+1/2,j,k}} + \delta_\zeta\phi_{i+1/2,j,k}\ S_{\zeta x_{i+1/2,j,k}}}{V_{i+1/2,j,k}} \tag{8}$$

where δ_ξ, δ_η, δ_ζ denote central difference operators in the curvilinear coordinate directions. In practice, coordinate grids for the resolution of viscous shear layers are highly stretched in

the direction normal to the layer and therefore, an one-dimensional error analysis of the discrete approximation to the viscous terms can give useful insight. In [4], it was shown that the present scheme is first-order accurate on general stretched meshes and second-order accuracy is obtained on smoothly stretched meshes. In the present version of the code, the viscous terms have been simplified by taking into account gradients in the direction normal to the viscous shear layers only (thin layer approximation).

In order to prevent odd-even point decoupling and oscillations near shock waves, artificial dissipative terms are added to the governing discrete equations. The artificial dissipation model considered in this paper is based on the work of Jameson, Schmidt and Turkel [1]. A blend of fourth and second differences is used to provide third-order background dissipation in smooth regions of the flow and first-order dissipation at shock waves, and is given by

$$\vec{D}_{i,j,k} = (D^2_\xi - D^4_\xi + D^2_\eta - D^4_\eta + D^2_\zeta - D^4_\zeta)\,\vec{W}_{i,j,k} \,. \tag{9}$$

The second and fourth difference operators read

$$D^2_\xi\,\vec{W}_{i,j,k} = \nabla_\xi(\overline{\lambda}_{\xi\ i+1/2,j,k}\cdot\varepsilon^{(2)}_{i+1/2,j,k})\Delta_\xi\vec{W}_{i,j,k} \,, \tag{10}$$

$$D^4_\xi\,\vec{W}_{i,j,k} = \nabla_\xi(\overline{\lambda}_{\xi\ i+1/2,j,k}\cdot\varepsilon^{(4)}_{i+1/2,j,k})\Delta_\xi\nabla_\xi\Delta_\xi\vec{W}_{i,j,k} \,, \tag{11}$$

where Δ_ξ, ∇_ξ are forward and backward difference operators in the ξ-direction. In order to avoid excessively large dissipation levels for cells with high aspect ratios and to maintain good damping properties of the scheme, a variable scaling factor of the dissipative terms is employed, which is a function of the spectral radii of the Jacobian matrices associated with the ξ,η,ζ directions and accounts for varying cell aspect ratio

$$\overline{\lambda}_{\xi\ i+1/2,j,k} = \lambda_{\xi\ i+1/2,j,k}\cdot\Phi_{i+1/2,j,k} \,, \tag{12}$$

$$\Phi_{i+1/2,j,k} = 1 + \max((\lambda_{\eta\ i+1/2,j,k}/\lambda_{\xi\ i+1/2,j,k})^\omega\,,\,(\lambda_{\zeta\ i+1/2,j,k}/\lambda_{\xi\ i+1/2,j,k})^\omega) \,,$$

$$\lambda_{\xi\ i+1/2,j,k} = |\vec{u}_{i+1/2,j,k}\cdot\vec{S}_{\xi\ i+1/2,j,k}| + c\,|\vec{S}_{\xi\ i+1/2,j,k}| \,,$$

$$\lambda_{\eta\ i+1/2,j,k} = |\vec{u}_{i+1/2,j,k}\cdot\vec{S}_{\eta\ i+1/2,j,k}| + c\,|\vec{S}_{\eta\ i+1/2,j,k}| \,,$$

$$\lambda_{\zeta\ i+1/2,j,k} = |\vec{u}_{i+1/2,j,k}\cdot\vec{S}_{\zeta\ i+1/2,j,k}| + c\,|\vec{S}_{\zeta\ i+1/2,j,k}| \,,$$

where $\vec{u}_{i+1/2,j,k}$ denotes the velocity vector and c is the speed of sound. The use of the maximum function in the definition of Φ is important for grids where λ_η/λ_ξ and $\lambda_\zeta/\lambda_\xi$ are very large and of same order of magnitude. In this case, if these ratios are summed rather than taking the maximum, too large dissipative terms are obtained, which may destroy the convergence of the time-stepping scheme. In general, coordinate grids around three-dimensional configurations exhibit larger variations of the cell aspect ratio than two-dimensional grids. Therefore, we have observed somewhat less freedom in the choice of the exponent ω in three dimensions. It has been found that the choice ω=0.5 yields a robust three-dimensional scheme.

The coefficients $\varepsilon^{(2)}$ and $\varepsilon^{(4)}$ use the pressure as a sensor for shocks in the flow field. They are defined as

$$\varepsilon^{(2)}_{i+1/2,j,k} = k^{(2)}\max(\nu_{i-1,j,k},\nu_{i,j,k},\nu_{i+1,j,k},\nu_{i+2,j,k}) \tag{13}$$

$$\nu_{i,j,k} = \left| \frac{p_{i-1,j,k} - 2p_{i,j,k} + p_{i+1,j,k}}{p_{i-1,j,k} + 2p_{i,j,k} + p_{i+1,j,k}} \right|$$

$$\varepsilon^{(4)}_{i+1/2,j,k} = \max(\,0\,,\,(k^{(4)} - \varepsilon^{(2)}_{i+1/2,j,k}))$$

where $k^{(2)}$ and $k^{(4)}$ are constants. The dissipation operators in the η- and ζ-directions are defined in a similar manner.

Boundary Conditions

At subsonic inflow/outflow boundaries, locally one-dimensional flow normal to the boundary is assumed. According to [8], the governing flow equations are linearized around the values at the end of the previous time step, and the characteristic variables corresponding to outgoing characteristics are extrapolated from the interior. The characteristic variables corresponding to incoming characteristics are determined from the free stream.

For two-dimensional flows around airfoils, it is well known that the free-stream conditions have to be specified by taking into account the circulation around the airfoil to obtain correct values of lift and drag for a given angle of attack. The influence of an improper determination of the free stream at the far field may be felt even if the distance to the far field is as large as 20-50 chord lengths. The usual practice in calculating the free-stream conditions for flows around finite-span wings has been to use simply the undisturbed onset flow conditions. In fact, if the far field is sufficiently far away from the wing surface, the disturbances created by the wing behave like those coming from a point singularity rather than a line singularity as in two-dimensional flow. Hence, a disturbance would decay more rapidly in three-dimensional flow than in two-dimensional flow, thus allowing the use of a smaller distance to the far-field.

More accurate results can be expected if the free-stream conditions used in three-dimensional flow computations take into account disturbances created by the aerodynamic surfaces. Klunker [9] shows that the small-disturbance potential at the far field is dominated by terms representing the lift of the aerodynamic surface. He derives an equation in which the potential at the far field is determined by integrating the contributions of singularities representing the local circulation over the entire wing surface. This approach has been used in [10] to determine the free-stream conditions in an Euler code.

If free-stream conditions are to be specified for general configurations a numerical integration over the aerodynamic surface for each point in the far field seems to be untractable. In particular, if multiblock structured meshes are to be used, this integration requires considerable amounts of programming effort and storage. The determination of the free stream is much simpler if the wing is replaced by a horse-shoe vortex. The components of the

disturbance velocity vector induced by a horse-shoe vortex in compressible flow are*

$$u = \frac{\beta^2\Gamma}{2\pi}\frac{y}{x^2+\beta^2y^2}\left[\frac{z+a}{\sqrt{\psi_+}}-\frac{z-a}{\sqrt{\psi_-}}\right] \tag{14}$$

$$v = \frac{-\Gamma}{2\pi}\left[\frac{z+a}{(z+a)^2+y^2}\left(1+\frac{x}{\sqrt{\psi_+}}\right)-\frac{z-a}{(z-a)^2+y^2}\left(1+\frac{x}{\sqrt{\psi_-}}\right)+\frac{\beta^2x}{x^2+\beta^2y^2}\left(\frac{z+a}{\sqrt{\psi_+}}-\frac{z-a}{\sqrt{\psi_-}}\right)\right] \tag{15}$$

$$w = \frac{\Gamma}{2\pi}\left[\frac{y}{(z+a)^2+y^2}\left(1+\frac{x}{\sqrt{\psi_+}}\right)-\frac{y}{(z-a)^2+y^2}\left(1+\frac{x}{\sqrt{\psi_-}}\right)\right] \tag{16}$$

where

$$\beta = \sqrt{1 - M_\infty{}^2}\,,$$

$$\psi_+ = x^2+\beta^2(z+a)^2 + \beta^2y^2\,,$$

$$\psi_- = x^2+\beta^2(z-a)^2 + \beta^2y^2\,.$$

The circulation of the vortex is related to the lift of the wing by

$$\Gamma=\frac{V_\infty}{2}c_{mean}C_L\,, \tag{17}$$

the quantity a denotes the half span of the horse-shoe vortex and c_{mean} is the mean chord of the wing. The position of the horse-shoe vortex with respect to the Cartesian coordinates x,y,z is shown in Fig. 3. The induced velocity is infinite downstream of the wing where the vortex crosses the boundary. In reality, however, this is by no means a special point in the flow field. Furthermore, numerical experience indicates that the treatment of the outflow boundary downstream of the wing has no significant influence on the results. Therefore, the following numerical treatment has been employed. The denominators in (15) and (16) which are responsible for the singular behavior of v and w at downstream boundaries, are limited in their value for $x>0$, i.e. $(z+a)^2+y^2$ and $(z-a)^2+y^2$ are kept at values larger than a/2 for $x>0$. This means that the induced velocities are artificially reduced in their value within the distance a/2 around the vortex line which crosses the downstream far-field boundary.

For all grid points at the far field, the geometric relations in the formulas given above can be evaluated once and stored. At each time step, these influence coefficients are multiplied by the total lift of the wing and added to the onset flow. Thus, the work to obtain the free-stream velocities is negligible. The pressure and the density of the free stream are then obtained using the assumption of isentropic flow and constant total enthalpy. The numerical results obtained with the present determination of the free-stream values show a reduced sensitivity to the far-field distance (see section on numerical results).

* These relations have been derived in unpublished 'Notes on Linearized Subsonic Wing Theory' by E.B. Klunker and K.C. Harder.

At solid walls, the no-slip condition is enforced by setting

$$u = v = w = 0 \tag{18}$$

The continuity and energy equations are solved at the grid points lying on the surface assuming an adiabatic wall. For this purpose, a control volume is formed with the four nearest cells outside and their mirror images inside. When updating the convective terms, the flow variables at the computational points inside are obtained as the symmetric images of the values outside. For the viscous terms, the density and the total energy inside are obtained as symmetric images, whereas the velocity components are taken as the antisymmetric images of the values just outside.

It has been found that the computed velocity distributions near the wall may be significantly affected by the artificial dissipative terms if the stencil of the dissipative terms normal to the wall is not properly defined. The reasons for this are the high grid stretching normal to the wall and the steep velocity gradients of the turbulent boundary layer. When solving the momentum equations at the grid point just outside the wall at j=3, the dissipation operator needs the dependent variables just inside. The extrapolation formula

$$\Delta_\eta \vec{W}_{i,1,k} = \vec{W}_{i,2,k} - \vec{W}_{i,1,k} = 2\,\Delta_\eta \vec{W}_{i,2,k} - \Delta_\eta \vec{W}_{i,3,k} \tag{19}$$

rather than the usual linear form

$$\Delta_\eta \vec{W}_{i,1,k} = \Delta_\eta \vec{W}_{i,2,k} \tag{20}$$

results in much less sensitivity of the solution to artificial viscosity and has had no significant drawback on convergence in the computations made so far.

Time Stepping Scheme

The system of ordinary differential equations which is obtained by the discretization in space is advanced in time with a five-stage Runge-Kutta scheme. A hybrid scheme is used where the physical viscous terms are computed on the first stage and frozen for the remaining stages and the artificial dissipative terms are evaluated on the first, third and fifth stages of the scheme. At the (m+1)st stage,

$$\vec{W}^{(m+1)} = \vec{W}^{(0)} - \alpha_{m+1}\Delta t \left[\vec{Q}^{(m)} - \sum_{n=0}^{m} \gamma_{mn}\vec{D}^{(n)}\right], \tag{21}$$

$$\vec{Q}^{(m)} = \vec{Q}_c^{(m)} + \vec{Q}_v^{(m)} .$$

where $\vec{W}^{(0)}$ is the solution at the old time level, and Δt is the time step. The subscripts c and v refer to convection and physical diffusion contributions to the discrete flow equations. The stage coefficients, α_m are taken as

$$\alpha_1 = 1/4, \quad \alpha_2 = 1/6, \quad \alpha_3 = 3/8, \quad \alpha_4 = 1/2, \quad \alpha_5 = 1 . \tag{22}$$

The weighting factors of the artificial dissipation satisfy the condition

$$\sum \gamma_{mn} = 1 \ . \tag{23}$$

They are

$$\begin{gathered}
\gamma_{00} = 1 \\
\gamma_{10} = 1 \ , \quad \gamma_{11} = 0 \ , \\
\gamma_{20} = (1-\bar{\gamma}_3) \ , \quad \gamma_{21} = 0 \ , \quad \gamma_{22} = \bar{\gamma}_3 \ , \\
\gamma_{30} = (1-\bar{\gamma}_3) \ , \quad \gamma_{31} = 0 \ , \quad \gamma_{32} = \bar{\gamma}_3 \ , \quad \gamma_{33} = 0 \ , \\
\gamma_{40} = (1-\bar{\gamma}_3)(1-\bar{\gamma}_5) \ , \quad \gamma_{41} = 0 \ , \quad \gamma_{42} = \bar{\gamma}_3(1-\bar{\gamma}_5) \ , \\
\gamma_{43} = 0 \ , \quad \gamma_{44} = \bar{\gamma}_5 \ ,
\end{gathered} \tag{24}$$

where $\bar{\gamma}_3 = 0.56$, $\bar{\gamma}_5 = 0.44$. It has been shown in [3], that this scheme has a particularly large parabolic stability limit. The steady-state solution is independent of the time step and therefore, the scheme is amenable to convergence acceleration techniques.

Three methods are employed to accelerate convergence of the basic explicit time stepping scheme. These techniques are as follows: (1) local time stepping, (2) implicit residual smoothing and (3) multigrid.

With local time stepping, the solution at each mesh point is advanced at the maximum Δt allowed by stability. Both convection and diffusion stability limits are included in the computation of Δt as

$$\Delta t = \mathrm{CFL} \frac{V^2}{V(\lambda_\xi+\lambda_\eta+\lambda_\zeta) + c_{diff}\nu_{diff}(\vec{S}_\xi\cdot\vec{S}_\xi + \vec{S}_\eta\cdot\vec{S}_\eta + \vec{S}_\zeta\cdot\vec{S}_\zeta)} \ , \tag{25}$$

where

$$\nu_{diff} = \max\left(\frac{4}{3}, \frac{\gamma}{Pr}\right) \frac{\mu+\mu_t}{\rho} \ ,$$

and the coefficient $c_{diff} = 2$ is used.

The stability range of the basic time stepping scheme can be extended using implicit smoothing of the residuals [11]. For three-dimensional flows the residual smoothing is applied in the form

$$(1-\varepsilon_\xi\nabla_\xi\Delta_\xi)(1-\varepsilon_\eta\nabla_\eta\Delta_\eta)(1-\varepsilon_\zeta\nabla_\zeta\Delta_\zeta)\ \bar{R}_m = R_m \tag{26}$$

where R_m is the explicit residual at the Runge-Kutta stage m in (21), and $\bar{R}_m$ is the final residual at stage m after the sequence of smoothing in the ξ, η and ζ directions.

The use of constant coefficients in the implicit treatment has proven to be satisfactory (extending the CFL number by a factor of two to three) even for meshes with cells of high aspect ratio, provided additional support such as enthalpy damping [1] is introduced. However, the use of enthalpy damping, which assumes constant total enthalpy throughout the flow

field, precludes the solution of problems with heat transfer effects. The need for enthalpy damping can be eliminated by using variable coefficients ε_ξ, ε_η, and ε_ζ that account for the variation of the cell aspect ratio.

For this purpose, consider a cell where the edge lengths in the ξ- and ζ- directions are much longer than that in the η-direction. The explicit time step is limited by the characteristic wave speed in the direction of the short cell edge. It is obvious that, for an extension of stability, implicit smoothing is required in the η-direction. If the same implicit residual smoothing is also applied in the other directions, where the characteristic wave speeds are much smaller than the stability limit, the damping behavior of the scheme, which is optimal at wave speeds near the stability limit, is impaired. To overcome this problem, Martinelli [3] has given a formula, in which the smoothing coefficient is a function of the characteristic wave speeds. Martinelli's form and variable smoothing coefficients in general are discussed in detail in the unpublished work of Swanson. Here, it is extended to three dimensions, i.e. ε_ξ may be defined as

$$\varepsilon_\xi = \max\left(0\ ,\ \frac{1}{4}\left(\frac{\mathrm{CFL}}{\mathrm{CFL}_{\mathrm{explicit}}}\frac{\lambda_\xi}{\lambda_\xi+\max(\lambda_\eta,\lambda_\zeta)}\left(1+\max\left(\left(\frac{\lambda_\eta}{\lambda_\xi}\right)^\omega,\left(\frac{\lambda_\zeta}{\lambda_\xi}\right)^\omega\right)\right)\right)^2-1\right)\ . \tag{27}$$

Finally, a multigrid method is employed which is based on the work of Jameson [2]. For the multigrid process, coarser meshes are obtained by eliminating every other mesh line in each coordinate direction. The solution is transferred to coarser meshes by injection. Residuals are transferred from fine to coarse meshes by a weighted average over the fine mesh grid points which are nearest to the point on the coarse mesh. A forcing function is constructed so that the solution on a coarse mesh is driven by the residuals collected on the next finer mesh. This procedure is repeated on each succeeding coarser mesh until the coarsest mesh is reached. Then, the corrections are transferred to the next finer mesh by trilinear interpolation. A fixed W-type cycle is used to execute the multigrid strategy. The robustness of the multigrid scheme is greatly improved by smoothing the total corrections before the solution is updated. That is,

$$\vec{W}^{(n+1)} = \vec{W}^n+\Delta\vec{W}_{\mathrm{tot}} \tag{28}$$

where

$$\Delta\vec{W}_{\mathrm{tot}} = \Delta\vec{W}_F + \Delta\vec{W}_C\ .$$

The quantity $\Delta\vec{W}_F$ is the solution correction from the finest grid, and $\Delta\vec{W}_C$ is the resultant solution correction from the coarse grids. The smoothing reduces high frequency oscillations introduced by the linear interpolation of the coarse mesh corrections and hence, convergence of the scheme is obtained for a much broader range of dissipation coefficients. The factored scheme of (26) with constant coefficients ($\varepsilon_\xi = \varepsilon_\eta = \varepsilon_\zeta = 0.2$) is used for this smoothing. Additional robustness and efficiency of the multigrid scheme is achieved by computing more than a single time step on the coarse meshes. In the first place, the use of multiple time steps on the coarse meshes improves the convergence, because the solution is further advanced in

time on the coarse meshes. Secondly, multiple time stepping improves the damping characteristics on the coarse meshes. Thus, smaller values of coarse-mesh dissipation may be used which results in an improvement of the convergence to the steady state. Finally, the application of a Full Multigrid method provides a well conditioned starting solution for the finest mesh being considered.

Turbulence Models

In the present work two turbulence models are considered. The first model is the widely used algebraic model of Baldwin and Lomax [12], which is based on the eddy viscosity hypothesis. The eddy viscosity is defined as

$$\mu_t = \min(\mu_{t,i}, \mu_{t,o}) \, . \tag{29}$$

In the inner region of the boundary layer,

$$\mu_{t,i} = \rho(\kappa \, D \, d)^2 \, \Omega \tag{30}$$

where κ is von Karman's constant, Ω is the magnitude of the vorticity, and the coordinate d is the distance from the wall. The quantity D is the van Driest damping factor

$$D = 1 - \exp(-y^+/26), \quad y^+ = d\frac{\sqrt{\rho_w \tau_{l,max}}}{\mu_w} \, . \tag{31}$$

Note, that the maximum laminar shear stress across the layer, $\tau_{l,max}$ rather than the shear stress at the wall is used to define the damping term in order to prevent vanishing eddy viscosity at the separation points. In the outer region,

$$\mu_{t,o} = 1.6 \cdot 0.0168 \rho F_{wake} \gamma \, , \tag{32}$$

where

$$F_{wake} = \min(d_{max}F_{max}, d_{max}U_{dif}^2/F_{max}) \, . \tag{33}$$

F_{max} is the maximum value of

$$F = D \, \Omega \, d \tag{34}$$

across the layer, and d_{max} is the value of d at which it occurs. The quantity U_{dif} is the difference of the flow speed across the shear layer. The intermittency factor γ is

$$\gamma = \frac{1}{1+5.5(0.3 \cdot d/d_{max})^6} \tag{35}$$

This turbulence model will be denoted by B.-L..

Frequently, it has been observed that in separated flows, the assumption of an equilibrium of the turbulence is not valid. Both convection and diffusion of turbulence have to be taken into account to allow for a more accurate determination of the turbulent stresses. For this purpose, Johnson and King [6] have devised an extended eddy viscosity model for separated wall boundary layers. They postulate that the viscosity of the inner layer near the

wall and the shape of the eddy-viscosity distribution in the outer layer may be accurately described with algebraic relations assuming equilibrium. The equilibrium distribution of the outer layer, however, is multiplied with a nonequilibrium factor in such a way that a transport equation for the maximum shear stress in the layer is fulfilled. Thus, the complete model is a nonequilibrium model of turbulence. In the following, a slightly modified version of this model is described. The model is particularly convenient for use in three-dimensional Navier-Stokes codes by using the Baldwin-Lomax formulation for the outer viscosity as proposed in [13].

First, instead of using the maximum turbulent shear stress as originally proposed in [6], a turbulence reference quantity,

$$g_m = (\Omega\, \mu_t/\rho)_m \tag{36}$$

is introduced, where the index m denotes the maximum of g across the shear layer. Note, that g_m is invariant to the coordinate system used, and therefore, it can be easily used in Navier-Stokes codes. According to [6], the eddy viscosity is defined by an exponential blending of the inner and the outer viscosity

$$\mu_t = \mu_{t,o}\left[1-\exp\frac{\mu_{t,i}}{\mu_{t,o}}\right]. \tag{37}$$

The inner viscosity is written as

$$\mu_{t,i} = \rho D^2\, \kappa\, d\, g_m^{1/2}\,, \tag{38}$$

$$D = 1-\exp\left[\frac{-d\,\sqrt{\rho_w \max(\rho_w g_m,\, \tau_w)}}{A^+\mu_w}\right].$$

The use of the maximum function in (38) is important for numerical stability on coarse meshes, where the turbulent boundary layer is not well resolved. According to [14], a value of 17 has been chosen for A^+. In the outer layer, the original model of Johnson and King uses the flow velocity at the edge of the boundary layer and the displacement thickness to define the outer viscosity. The displacement thickness, however, is not easily determined in three-dimensional flows. In order to avoid numerical problems associated with searching through the boundary layer in three-dimensional flows, the viscosity in the outer layer is determined by the relation of Baldwin and Lomax

$$\mu_{t,o} = \sigma\; 1.6 \cdot 0.0168\rho F_{wake}\gamma\,. \tag{39}$$

The quantity σ is the aforementioned nonequilibrium factor, and F_{wake} is defined according to (33). The intermittency factor, however, is redefined as

$$\gamma = \frac{1}{1+5.5(d/\delta)^6} \tag{40}$$

where δ denotes the thickness of the boundary layer. In [15] it has been demonstrated that

$$\delta = 1.9\, d_{max} \tag{41}$$

is a good approximation for wall boundary layers, and this relation is incorporated into the model. Furthermore, the behavior of the model in separated flow can be improved, if the distance d in (34) for the function F is computed according to Fig. 4 rather than taking the distance from the wall.

Assuming that g is proportional to the kinetic energy of turbulence, the distribution of g_m over the aerodynamic surface is determined by a differential equation given in [6]. For three-dimensional flows, the equation may be written as

$$\frac{\partial g_m}{\partial t}+u_m\frac{\partial g_m}{\partial x}+v_m\frac{\partial g_m}{\partial y}+w_m\frac{\partial g_m}{\partial z}+\frac{a_1\, g_m}{L_m}(g_m^{1/2}-g_{eq,m}^{1/2})+g_m^{3/2}D_m = 0\ . \tag{42}$$

Here, u_m, v_m, and w_m are the Cartesian velocity components at the location of g_m. The index eq,m denotes the equilibrium value at the location of g_m, and the length scale, L_m, is defined as

$$L_m = 0.4 d_m \quad \text{for} \quad d_m/\delta \le 0.225\ , \tag{43}$$

$$L_m = 0.09\delta \quad \text{for} \quad d_m/\delta > 0.225\ .$$

The diffusion term, D, is defined as

$$D = \frac{a_2\, \max(0,\, \sigma^{1/2}-1)}{\delta(0.7 - (d/\delta)_m)}\ . \tag{44}$$

The model constants a_1=0.25 and a_2=0.5 are used here. Equation (44) states that the diffusion of turbulence is neglected in retarded flows, where σ<1, whereas in recovering regions, the diffusion is assumed to be proportional to $\sigma^{1/2}-1$. If g_m is replaced with $\hat{g}_m=g_m^{-1/2}$, a linear equation is obtained as

$$\frac{\partial \hat{g}_m}{\partial t}+u_m\frac{\partial \hat{g}_m}{\partial x}+v_m\frac{\partial \hat{g}_m}{\partial y}+w_m\frac{\partial \hat{g}_m}{\partial z}+\frac{a_1}{2\, L_m}g_{eq,m}^{1/2}\,\hat{g}_m - \frac{1}{2}(D+\frac{a_1}{L_m}) = 0\ . \tag{45}$$

(45) is valid along a surface which is determined by the location of the maximum of the reference quantity g. For numerical convenience, (45) is solved on the surface grid of the aerodynamic body rather at the location of g_m. The misalignment between these surfaces creates errors in the convective terms of (45). These errors are reduced by replacing the velocity components u_m, v_m, and w_m in (45) by their projection onto the body surface. It is believed, that the remaining errors, which are due to the skewness of the grid lines crossing the shear layer, are small in comparison with the uncertainties present in the basic assumptions of this turbulence model. Note, that the time derivative in (45) is retained, so that a time stepping scheme can be used for the numerical solution. Using Gauss's theorem, a cell centered finite-volume discretization with central differencing is applied to (45). Because $\hat{g}_m$ does not vary normal to the surface, only a layer of one cell thickness around the surface is required to

solve (45). Fourth difference dissipative terms are used to damp the discrete equations. The explicit five-stage Runge-Kutta scheme (21) is used for time stepping. The linear source term in (45) is treated implicitly, and thus, CFL-numbers around 3 can be used. The convergence to the steady state is further enhanced by local time stepping. For the computation of flow cases with strong separation the turbulent viscosity should be rapidly adjusting to the flow field in order to allow for convergence. Therefore, 10 explicit time steps are executed at each time, when the turbulence model is updated. The computational time for the solution of (45) is very small in comparison with the total effort, because only a single equation for a quantity, which does not change normal to the surface, is involved.

Once values of g_m have been computed by the numerical solution of (45), they can be compared to values of g_m from (36). The ratio of both these values is then used to update σ, as described in [13]; and eventually, convergence is obtained. The nonequilibrium turbulence model described herein will be denoted with J.-K.-mod. .

Numerical Results

The cell-vertex multigrid scheme described here has been applied to a wide variety of two- and three-dimensional flows. The two-dimensional subsonic laminar flow around NACA 0012 airfoil at the free-stream Mach number, $M_\infty = 0.5$, the angle of attack, $\alpha = 0°$, and the Reynolds number based on the chord length $Re_\infty = 5000$ is considered first. A C-type coordinate mesh of 257x65 points is used, where 129 points are distributed over the airfoil surface. The first spacing away from the wall is $5x10^{-4}$ chord lengths. Fig. 5 shows the convergence history, the streamlines, and the distributions of pressure and skin friction. The computed values of pressure drag and skin-friction drag and the separation point agree well with the results of Swanson and Turkel [16]. The solution converges rapidly, and, noting additional convergence criteria given in Table 1, a sufficiently accurate solution is obtained in less than 40 multigrid cycles on the fine mesh.

The transonic turbulent flow over the RAE 2822 airfoil is used to demonstrate the convergence behavior and the accuracy of the method for high Reynolds number turbulent flows. A mesh of 385x65 points is used, where 257 points are distributed over the airfoil surface, and the first spacing away from the wall is 10^{-5} chord lengths. Frequently, a mesh with 321x65 points has been used also, which has the same distribution of grid points at the surface, but less points along the wake line. In Fig. 6, the convergence behavior is displayed for $M_\infty = 0.73$, $\alpha = 2.79°$, $Re_\infty = 6.5x10^6$. Fig. 6a shows the influence of the fourth-difference dissipation on the convergence of the solution. The robustness of the scheme is demonstrated by the fact that the dissipation coefficient is varied by an order of magnitude without destroying the convergence of the scheme. Note, that the results of Fig. 6a have been obtained using single time steps on the coarse meshes. The effect of multiple time steps on the coarse meshes is shown in Fig. 6b. If two time steps are used, the convergence is significantly improved, and a residual reduction of 10 orders of magnitude is obtained within 340 multigrid cycles on the fine mesh. The convergence criteria in Table 1 indicate that sufficiently

converged solutions are obtained within 40 multigrid cycles. Fig. 6c shows the convergence with the nonequilibrium model of turbulences, which is slightly slower than with the B.-L. model.

Next, the accuracy of the scheme is examined using a variation of the grid density. For this purpose, a coarser mesh of 193x33 points is created by omitting every other point in each coordinate direction. Additionally, a very fine mesh of 577x97 points has been used. The variation of the coefficients for lift, pressure drag, and friction drag with number of mesh points N is presented in Fig. 7. The effect of the second and fourth difference dissipation is also indicated. On coarse meshes, the discretization error is obviously dominated by artificial dissipation. The finer meshes allow the extrapolation of the coefficients to their values for an infinitely fine mesh. For the 385x65 mesh ($N^{-1} \approx 4.0 \times 10^{-5}$), the predicted lift is within 1.5 percent, the pressure drag is within 3 counts, and the friction drag is within 0.3 count of the extrapolated values. For the 577x97 mesh ($N^{-1} \approx 1.8 \times 10^{-5}$), the predicted lift is within 0.5 percent, the pressure drag is within 1 count, and the friction drag is within 0.1 count of the extrapolated values. Fig. 8 shows pressure and skin-friction distributions for different grid densities, with a comparison to the experimental data of [17]. The main features of the flow are essentially captured with the 193x33 mesh. The differences between the solutions on the 385x65 and 577x97 meshes are small.

In Fig. 9, the effect of the turbulence model is presented. For both the equilibrium B.-L. model and the nonequilibrium J.-K.-mod. model, the position of the shock and its strength agree fairly well with the experimental data. The measured lift coefficient, however, is in better agreement with the results of the J.-K.-mod. model than with B.-L. The skin friction distribution of the J.-K.-mod. computation shows relatively high values downstream of the shock, which are not observed experimentally. The high skin friction in the recovery region is caused by the definition of the inner viscosity, (38), which is scaled by the maximum of the quantity g rather than taking local quantities as in (30). The definition (38) should be refined in future work.

In the following, the behavior of the turbulence models is presented for test cases with strong separation, which have been used recently to compare various computer codes for viscous transonic airfoils [18]. In Fig. 10, the flow around the RAE 2822 airfoil at $M_\infty = 0.75$, $\alpha = 2.81°$, $Re_\infty = 6.5 \times 10^6$ is considered. With the B.-L. model, the shock location is predicted 8% of the chord length downstream of the experimental data. The agreement of computation and experiment is considerably improved, when the J.-K.-mod. model is used, however, there are still some differences remaining. The bump in the pressure distribution downstream of the shock, as obtained with the J.-K.-mod. model, indicates that the height of the separated region, as well as the recovery process downstream are somewhat overpredicted.

Similar trends are observed for the next test case, the NACA 0012 airfoil at $M_\infty = 0.799$, $\alpha = 2.26°$, $Re_\infty = 9.0 \times 10^6$. Fig. 11 shows much better agreement in pressure distributions and lift and drag values, when the J.-K.-mod. model is used instead of the B.-L.

Drag polars have been computed for the NACA 0012 airfoil at $M_\infty = 0.7$ and $Re_\infty = 9.0x10^6$. The results of these computations are shown in Fig. 12 (lift versus angle of attack) and Fig. 13 (lift versus drag). Experimental results of Harris [19] with wind-tunnel corrections included are also displayed. Good agreement of computations and measurements is obtained at lower angles of attack. At high angles, the B.-L. model yields considerably higher lift values, than the J.-K.-mod. In particular, the J.-K.-mod. model predicts maximum lift with $C_{L,max} = 0.728$ at $\alpha = 6^o$, whereas the maximum lift is $C_{L,max} = 0.87$ at $\alpha = 7^o$ with the B.-L. model. There is no experimental value of the maximum lift for this particular Mach number given in [19]. The experimental values of the maximum lift at Mach numbers below and above, $C_{L,max} = 0.82$ for $M_\infty = 0.65$ and $C_{L,max} = 0.55$ for $M_\infty = 0.76$ indicate that the result of the J.-K.-mod. model is close to the probable result of the wind tunnel.

The last two-dimensional test case is the supersonic turbulent flow around NACA 0012 airfoil at $M_\infty = 2.0$, $\alpha = 0^o$, $Re_\infty = 10.0x10^6$. The convergence history and the distributions of pressure and skin friction are shown in Fig. 14. Generally, good convergence rates are obtained for Mach numbers up to 2. For higher Mach numbers, no solution could be obtained with the present scheme. In Fig. 15, the Mach contours and the mesh near the airfoil are shown. No attempt has been made to adapt the mesh to the bow shock, and therefore, the bow shock is not very well resolved in this computation.

The three-dimensional version of the code has been applied to the flow over the finite-span ONERA-M6 wing and to the three-dimensional flow over an airfoil mounted in the wind tunnel, where the viscous layer along the wind-tunnel side wall has been included in the simulation. In the present report, only the computations of transonic flows over the ONERA-M6 wing are presented. The results for the interaction between a wing and a side-wall boundary layer are given in a subsequent paper.

The computational domain around the wing is discretized using C-type topology in the streamwise direction and an O-type topology in the spanwise direction with 289x65x49 points. The distance to the first grid point away from the wall is 10^{-5} local chord lengths. The structure of the mesh is shown in Fig. 16a. There is considerable skewness in the wing-tip region, as indicated in Fig. 16b. A somewhat coarser mesh has been also used with 193x49x33 points. In the three-dimensional computations done so far, only a single time step is executed on the coarse meshes. Fig. 17 shows the convergence behavior of the three-dimensional scheme for M_∞=0.84 and Re_∞=11.x10^6. Two flow cases, namely $\alpha = 3.06^o$ with attached flow, and $\alpha = 6.06^o$ with a strong separation on the upper surface are considered. For the attached-flow case the influence of the fourth-difference dissipation on convergence is displayed in Fig. 17a. The convergence is not as good as for the two-dimensional cases. The largest residuals occur at the wing tip, where the grid is highly skewed. Therefore, a considerable improvement of the convergence can be expected, if the grid quality were improved in this region. The effect of multiple time steps on the coarse meshes for the attached-flow case is shown in Fig. 17b. The decrease of residuals versus multigrid cycles is not much affected

by multiple time stepping on the coarse meshes. Apparently, there are high frequency oscillations on the fine mesh, which are only slowly damped due to the grid skewness, and this behavior is not improved using more work on the coarse meshes. The convergence of the global flow field, however, is improved as shown in Table 1. The improvements which are obtained by multiple time stepping on the coarse meshes, are more pronounced for the separated flow case as shown in Fig. 17c. Here, the interaction process between the shock and the separating boundary layers is considerably accelerated, and converged values of lift and drag are obtained more rapidly, see Table 1.

Before examining details of the flow solution, it may be appropriate to look at the influence of the far-field distance on the lift and the drag of the wing. For this purpose, the distance to the far field is varied by omitting grid planes at the far field. The effect of determining the free-stream quantities by superimposing the flow field of a horse-shoe vortex to the onset flow is presented in Fig. 18. For far-field distances of 7 half spans, the results with and without vortex differ only by 0.3%. The variation of the distance to smaller values shows, that the use of the vortex reduces the sensitivity of lift and drag to the distance by about 50%. In the results given below, the distance to the far field is kept at 7 half spans, and the horse-shoe vortex terms are included.

The pressure distributions along several spanwise stations of the wing are displayed for the attached-flow case in Fig. 19. The results of the 289x65x49 mesh agree well with those from the coarser mesh and with experimental data [20]. From Table 1, it is evident, that the global features of the flow converge rapidly. Indeed, plots of the solution after 50 multigrid cycles, which are displayed in Fig. 20, show virtually no differences to the fully converged solution.

Results for the separated-flow case are displayed in Fig. 21. With the B.-L. turbulence model, large discrepancies between computation and experiment occur. The size of the separated region is underpredicted, and, consequently, the shock is located too far downstream. The agreement between computation and experimental data is greatly improved with the J.-K.-mod. model, Fig. 22. The size of the separated region and the location of the shock compare well with the data. The wall streamlines show a mushroom-type structure which is typical for wings at high angle of attack. Table 1 shows, that approximately 80 multigrid cycles on the fine mesh are sufficient for convergence to engineering accuracy. If the 193x49x33 grid is considered to be sufficiently fine, 80 multigrid cycles require less than 40 minutes CPU-time on the Cray-2 computer.

Concluding Remarks

A cell-vertex scheme for the Navier-Stokes equations, which is based on central difference approximations and Runge-Kutta time stepping, has been described. Using local time stepping, implicit residual smoothing with locally varying coefficients, a multigrid method, and carefully controlled artificial dissipative terms, very good convergence rates are obtained for a wide range of two- and three-dimensional flows. Details of the acceleration techniques, which

are important for convergence on meshes with high-aspect-ratio cells, have been discussed. In general, engineering accuracy is obtained within 40 multigrid cycles on the fine mesh for two-dimensional flows, and within 50-80 multigrid cycles in three dimensions. The accuracy of the code is examined by grid refinement studies and comparison with experimental data. For an accurate prediction of turbulent flows with strong separations, a modified version of the nonequilibrium turbulence model of Johnson and King is introduced, which is well suited for an implementation into three-dimensional Navier-Stokes codes. It is shown that the solutions for three-dimensional flows with strong separations can be dramatically improved, when a nonequilibrium model of turbulence is used.

Acknowledgement

The present work evolved within a scientific exchange program between DFVLR and NASA, while the author stayed at NASA Langley Research Center. The author gratefully acknowledges numerous discussions with M.D. Salas, Dr. R.C. Swanson, Dr. V.N. Vatsa. He is grateful to Dr. R. Abid for sharing his knowledge about the Johnson-King turbulence model. Furthermore, the author is indebted to C. Rossow for providing the cell-vertex Euler code as the basis of the present work, and to B.W. Wedan for generating the three-dimensional grids.

Langley Research Center
National Aeronautics and Space Administration
Hampton, VA 23665
December 15, 1988

References

[1] Jameson, A.; Schmidt, W.; Turkel, E.: Numerical Solutions of the Euler Equations by Finite Volume Methods Using Runge-Kutta Time- Stepping-Schemes. AIAA Paper 81-1259, (1981).

[2] Jameson, A.: Multigrid Algorithms for Compressible Flow Calculations. MAE Report 1743, Princeton University, Text of lecture given at 2nd European Conference on Multigrid Methods, Cologne, Oct. 1985, (1985).

[3] Martinelli, L.: Calculations of Viscous Flows with a Multigrid Method. Ph.D. Dissertation, MAE Department, Princeton University, (1987).

[4] Radespiel, R.; Swanson, R.C.: An Investigation of Cell Centered and Cell Vertex Multigrid Schemes for the Navier-Stokes Equations. AIAA Paper 89-0548, (1989).

[5] Jayaram, M.; Jameson, A.: Multigrid Solution of the Navier-Stokes Equations for Flows over Wings. AIAA Paper 88-0705, (1988).

[6] Johnson, D.A.; King, L.S.: A New Turbulence Closure Model for Boundary Layer Flows with Strong Adverse Pressure Gradients and Separation. AIAA Paper 84-0175, (1984).

[7] Rossow, C.-C.: Berechnung von Strömungsfeldern durch Lösung der Euler-Gleichungen mit einer neuen Finite-Volumen Diskretisierungsmethode. Dissertation TU-Braunschweig 1988.

[8] Whitfield, D.L.; Janus, J.M.: Three-Dimensional Unsteady Euler Equations Solution Using Flux Vector Splitting. AIAA Paper 84-1552, (1984).

[9] Klunker, E.B.: Contribution to Methods for Calculating the Flow about Thin Lifting Wings at Transonic Speeds - Analytic Expressions for the Far Field. NASA TN D-6530, (1971).

[10] Paisley, M.F.; Hall, M.G.: Improvements in the Formulation and Numerical Solution of the Euler Problem for Swept Wings. Symposium Transonicum III, DFVLR-AVA Göttingen, May 24-27 1988.

[11] Jameson, A.: The Evolution of Computational Methods in Aerodynamics. J. Appl. Mech., Vol. 50, (1983).

[12] Baldwin, B.S.; Lomax, H.: Thin Layer Approximation and Algebraic Model for Separated Turbulent Flows. AIAA Paper 78-257, (1978).

[13] Abid, R.; Vatsa, V.N.; Johnson, D.A.; Wedan, B.W.: Prediction of Separated Transonic Wing Flows with a Non-Equilibrium Algebraic Model. AIAA Paper 89-0558, (1989).

[14] Abid, R.: Extension of the Johnson-King Turbulence Model to the 3-D Flows. AIAA Paper 88-0223, (1988).

[15] Stock, H.W.; Haase, W.: The Determination of Turbulent Length Scales in Algebraic Turbulence Models for Attached and Slightly Separated Flows Using Navier-Stokes Methods. AIAA Paper 87-1302, (1987).

[16] Swanson, R.C.; Turkel, E.: Artificial Dissipation and Central Difference Schemes for the Euler and Navier-Stokes Equations. AIAA Paper 87-1107, (1987).

[17] Cook, P.H.; McDonald, M.A.; Firmin, M.C.P.: Aerofoil RAE 2822 - Pressure Distributions and Boundary Layer and Wake Measurements. AGARD-AR-138, (1979).

[18] Holst, T.L.: Viscous Transonic Airfoil Workshop Compendium of Results. AIAA Paper 87-1460, (1987).

[19] Harris, C.D.: Two-Dimensional Aerodynamic Characteristics of the NACA 0012 Airfoil in the Langley 8-Foot Transonic Pressure Tunnel. NASA TM 81927, (1981).

[20] Schmitt, V.; Charpin, F.: Pressure Distributions on the ONERA-M6-Wing at Transonic Mach Numbers. AGARD-AR-138, (1979).

CASE	GRID	TURBULENCE MODEL	NO. TIME STEPS ON COARSE MESH	1% C_L	0.1% C_L	S.S. PTS.	10^{-5} RED.	C_L	C_D
NACA 0012 M_∞=0.5 α = 0° Re=5000	257x65	---	2	4(13.4) *)	29(42) *)	---	83(104)	0.0	0.05544
RAE 2822 M_∞=0.73 α =2.79° Re=6.5x10^6	321x65	B.L.	2	14(32.9)	31(55.5)	41(68.9)	130(187.2)	0.8346	0.01727
ONERA M6 M_∞=0.84 α =3.06° Re=11x10^6	289x65x49	B.L.	1	6(886)	54(3745)	167(10412)	~460(27580)	0.2677	0.01782
ONERA M6 M_∞=0.84 α =3.06° Re=11x10^6	289x65x49	B.L.	2	4(810)	38(3204)	138(10244)	---	0.2677	0.01782
ONERA M6 M_∞=0.84 α =6.06° Re=11x10^6	289x65x49	J.-K.-Mod.	1	74(4944)	135(8482)	---	---	0.5085	0.05394
ONERA M6 M_∞=0.84 α =6.06° Re=11x10^6	289x65x49	J.-K.-Mod.	2	44(3638)	79(6102)	---	---	0.5085	0.05394

*) C_{DP} instead of C_L

Table 1 : Convergence behavior for two- and three-dimensional flows. Numbers denote the multigrid cycles on the fine mesh required to obtain the convergence criterion. Numbers in parenthesis are the total computation times in seconds on Cray-2. Coefficient of the fourth difference dissipation $K^{(4)} = 1/32$.

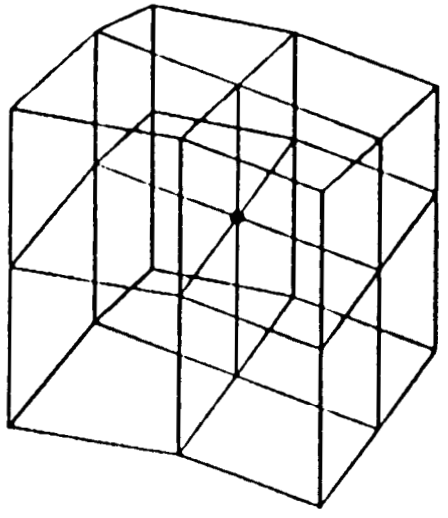

Fig. 1 : Control volume around point (i,j,k).

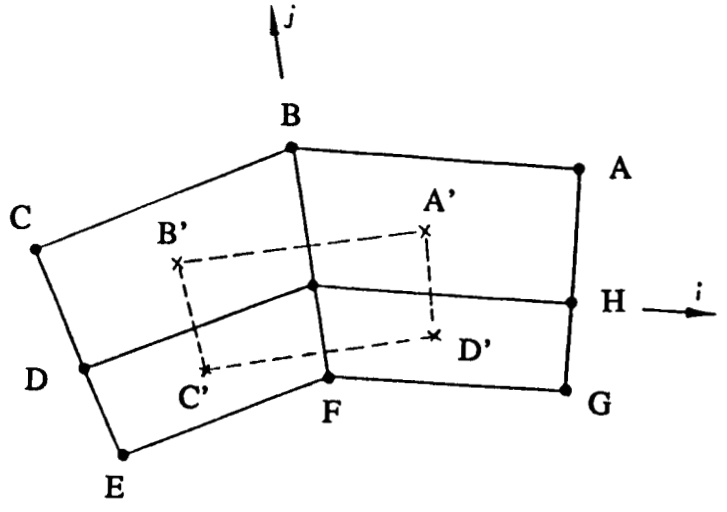

Fig. 2 : Control volume in a plane grid .

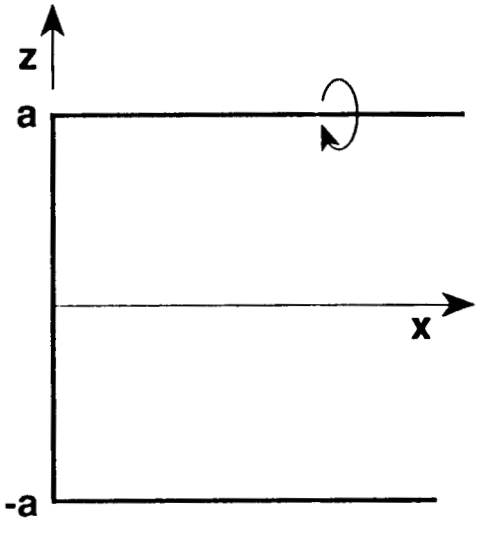

Fig. 3 : Definition of horse-shoe vortex with respect to cartesian coordinates .

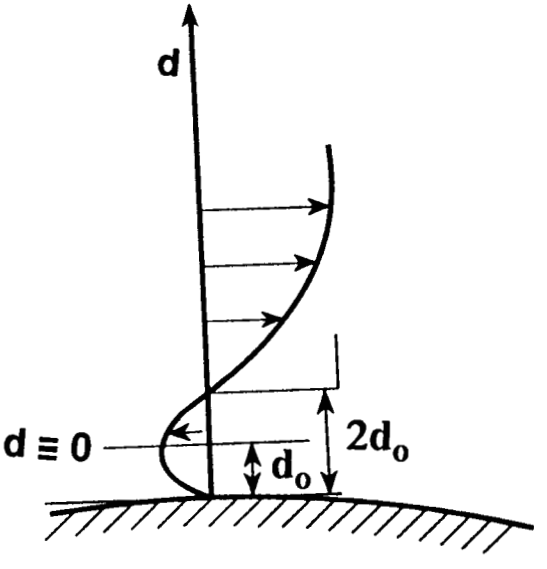

Fig. 4 : Definition of variable d in separated flow .

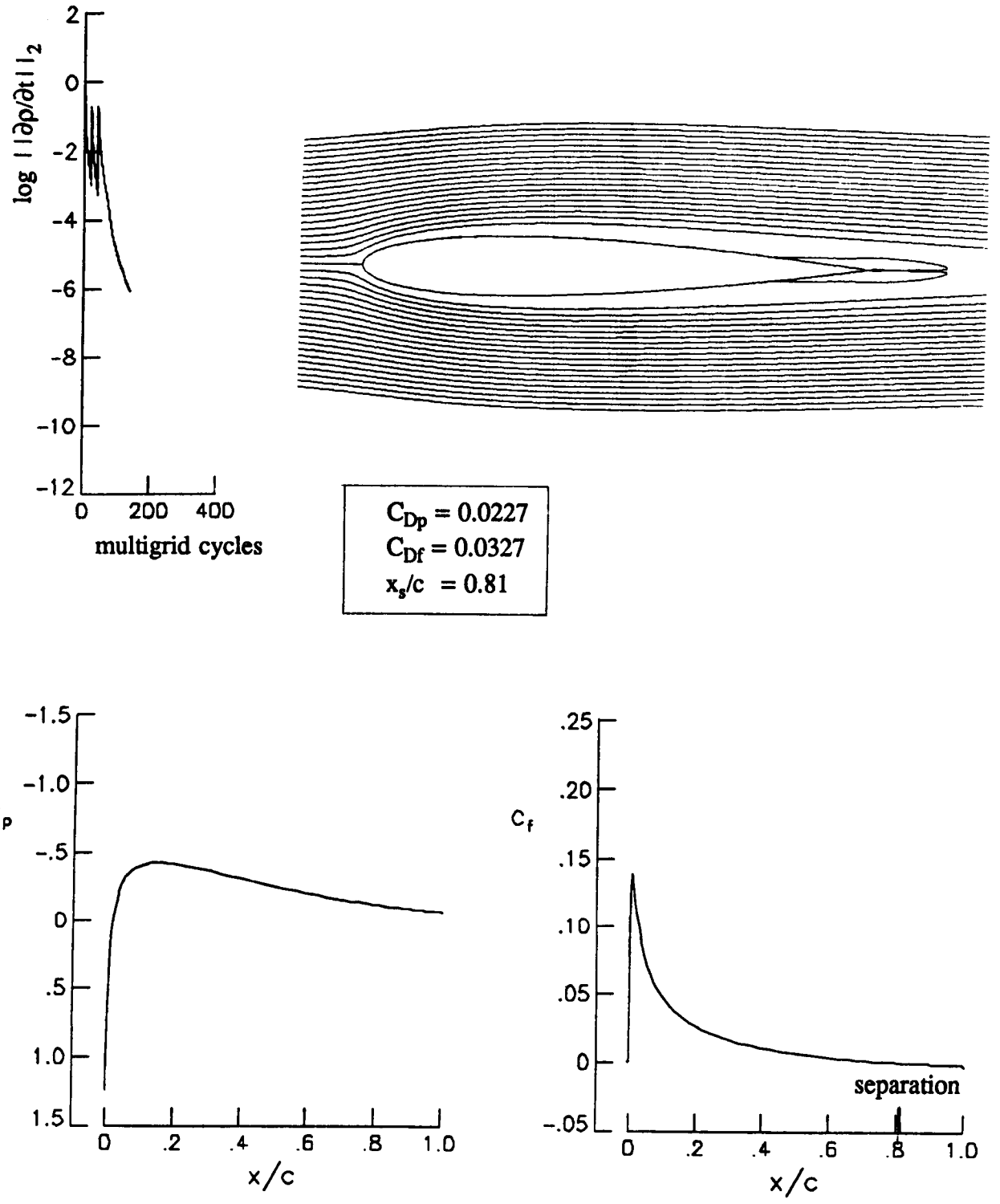

Fig. 5 : Convergence history, streamlines, and distributions of pressure and skin friction for laminar flow around NACA 0012 airfoil, M_∞=0.5, α=0°, Re_∞=5000, grid 257x65.

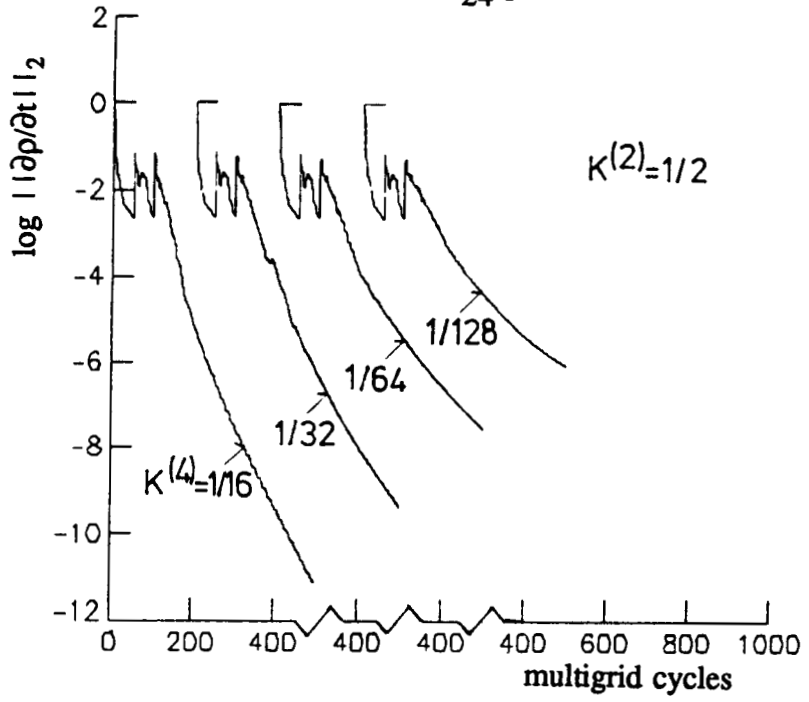

a) Influence of fourth-difference dissipation on convergence, single time step on coarse meshes, mesh 385x65, B.-L. model

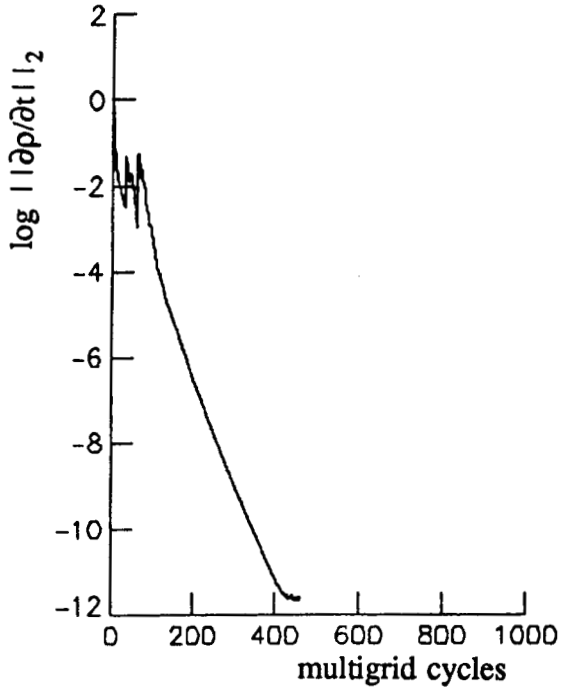

b) Convergence for two time steps on coarse meshes, $K^{(4)}$=1/32, mesh 321x65, B.-L. model

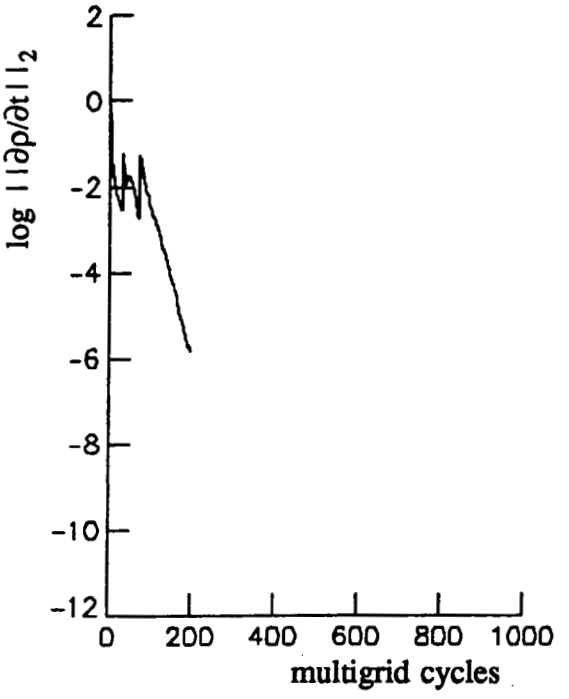

c) Convergence for nonequilibrium J.-K.-mod. turbulence model, two time steps on coarse meshes, $K^{(4)}$=1/32, mesh 321x65

Fig. 6 : Convergence behavior for transonic flow around RAE 2822 airfoil, M_∞=0.73, α=2.79° Re_∞=6.5x10^6).

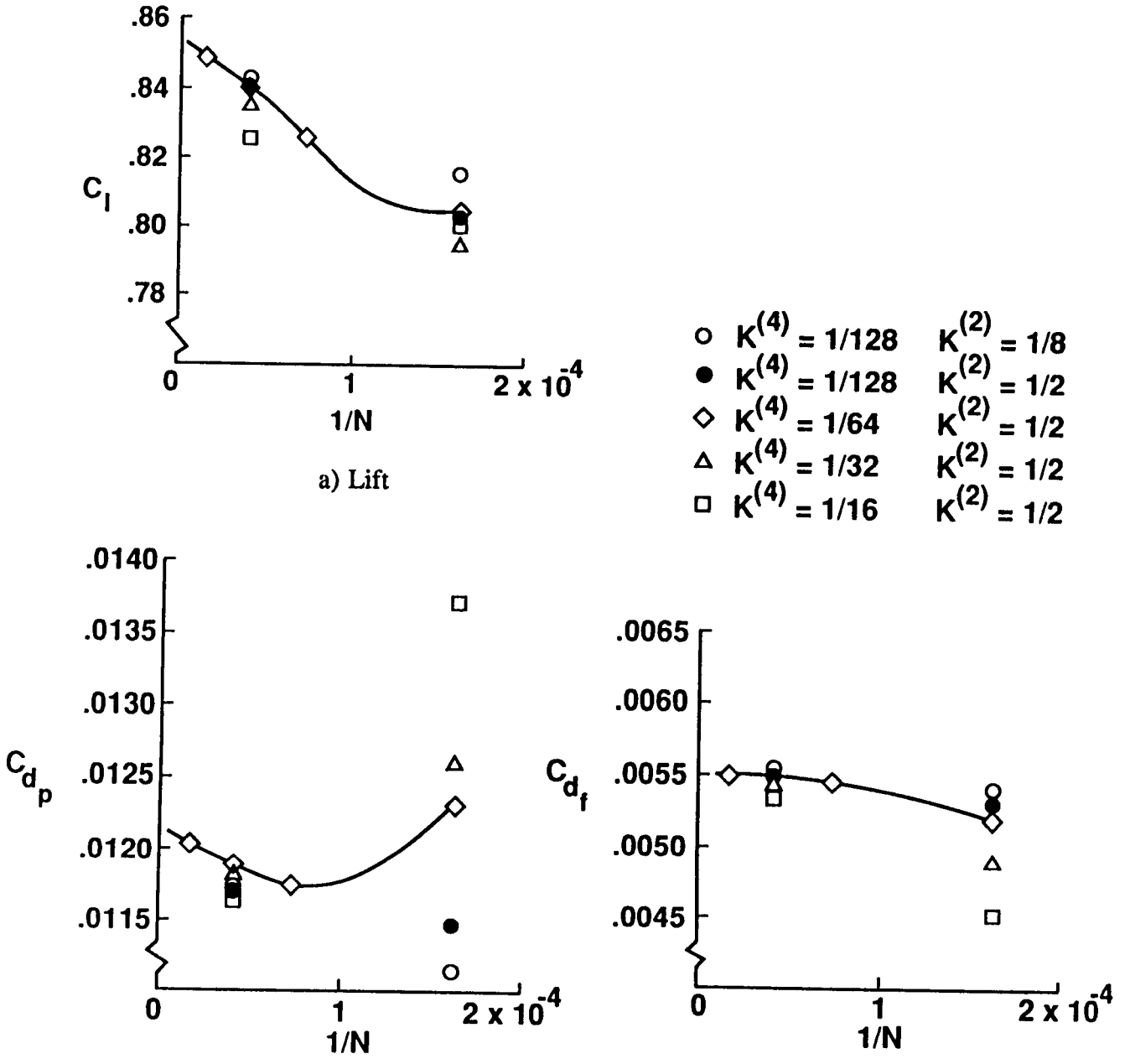

Fig. 7 : Influence of grid density and artificial viscosity on global force coefficients for flow around RAE 2822 airfoil (M_∞=0.73, α=2.79°, Re_∞=6.5x10^6), computed with B.-L. model.

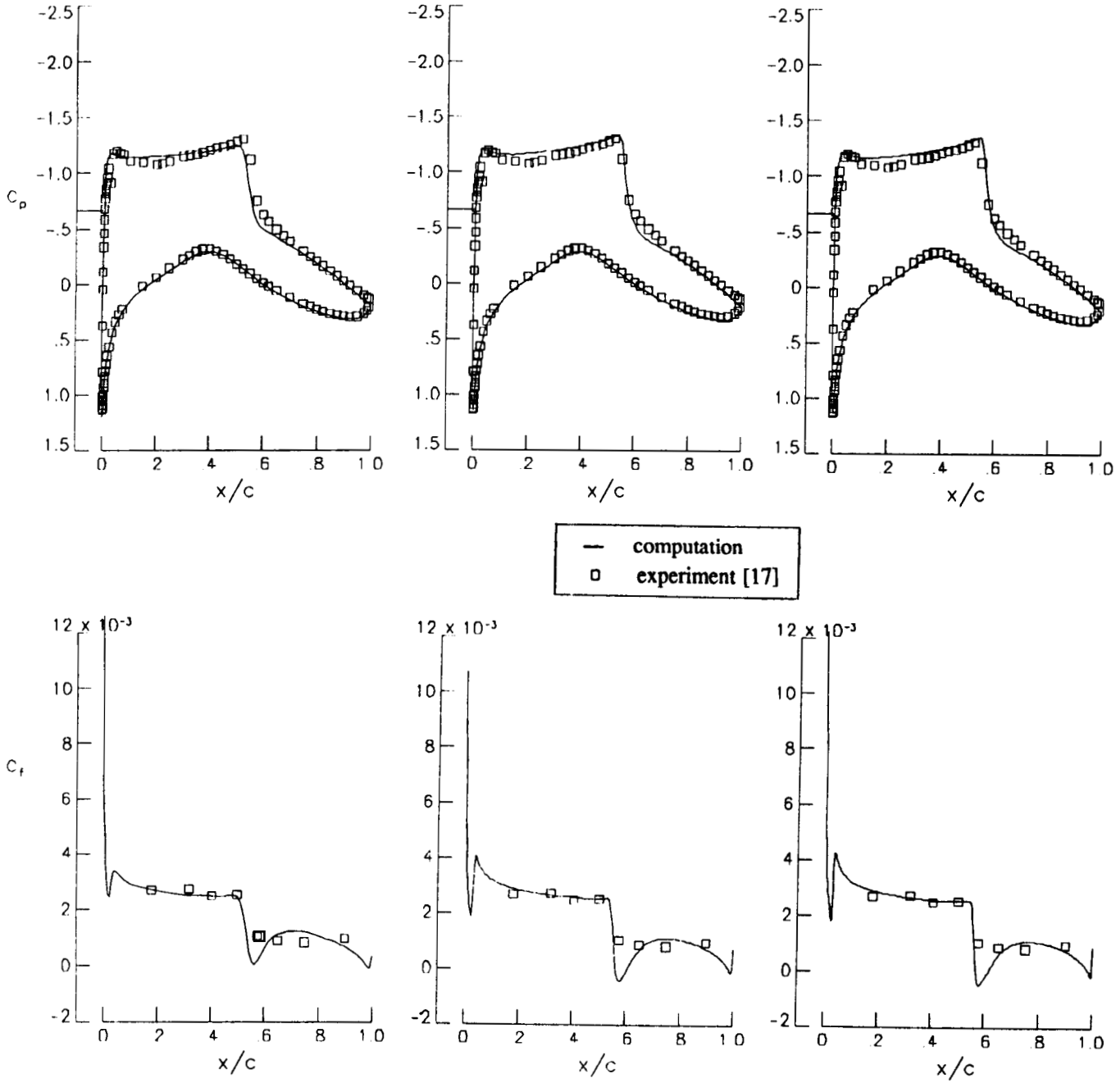

a) 193x33 grid b) 385x65 grid c) 577x97 grid

Fig. 8 : Distributions of pressure and skin friction for different grid densities (RAE 2822 airfoil, M_∞=0.73, α=2.79°, Re_∞=6.5x10^6, $K^{(4)}$=1/64), computed with B.-L. model .

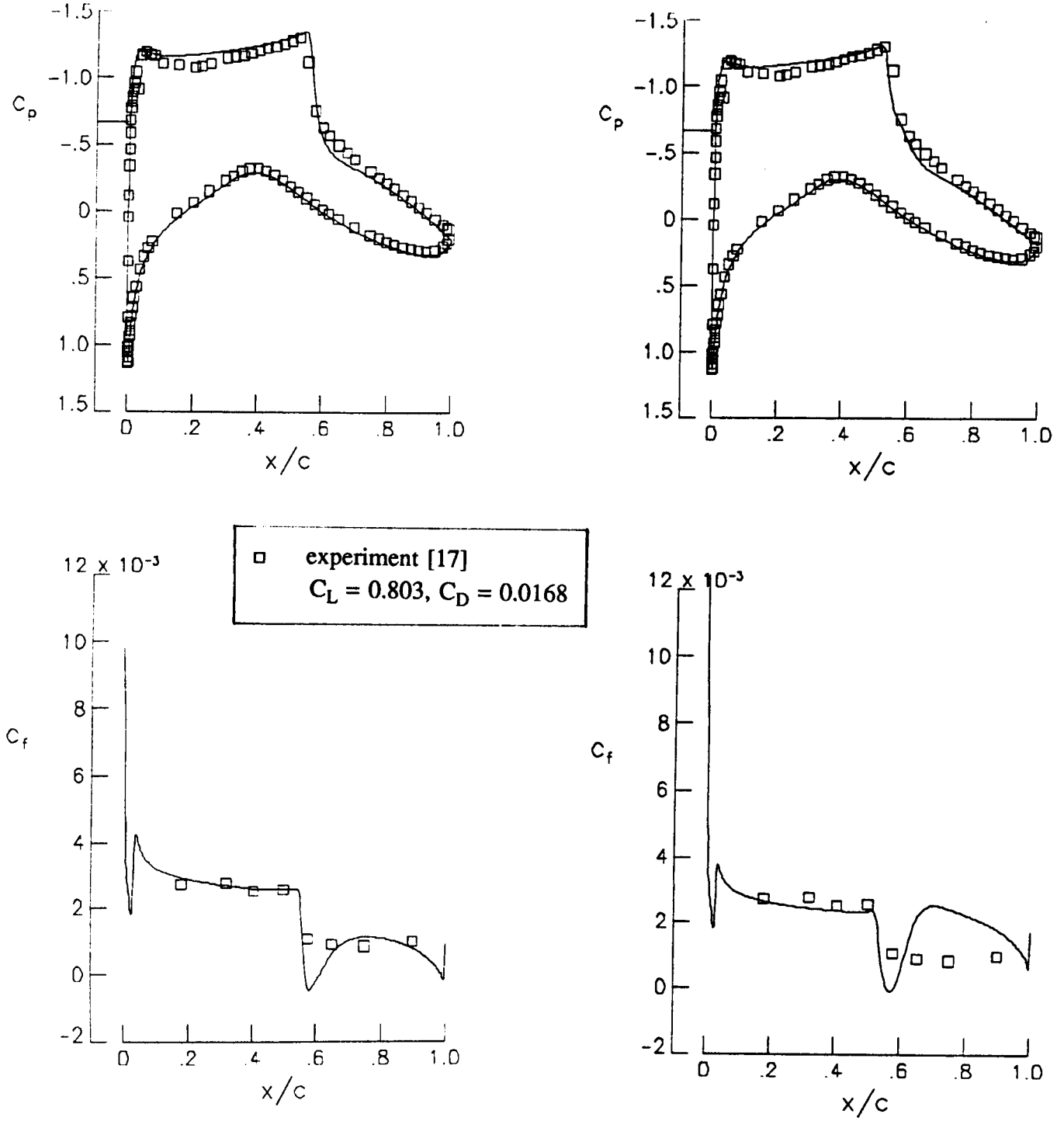

a) B.-L. model
C_L = 0.849, C_D = 0.0175

b) J.-K.-mod. model
C_L = 0.814, C_D = 0.0162

Fig. 9 : Effect of the turbulence model on distributions of pressure and skin friction for RAE 2822 airfoil (M_∞=0.73, α=2.79°, Re_∞=6.5x10^6, grid 481x97).

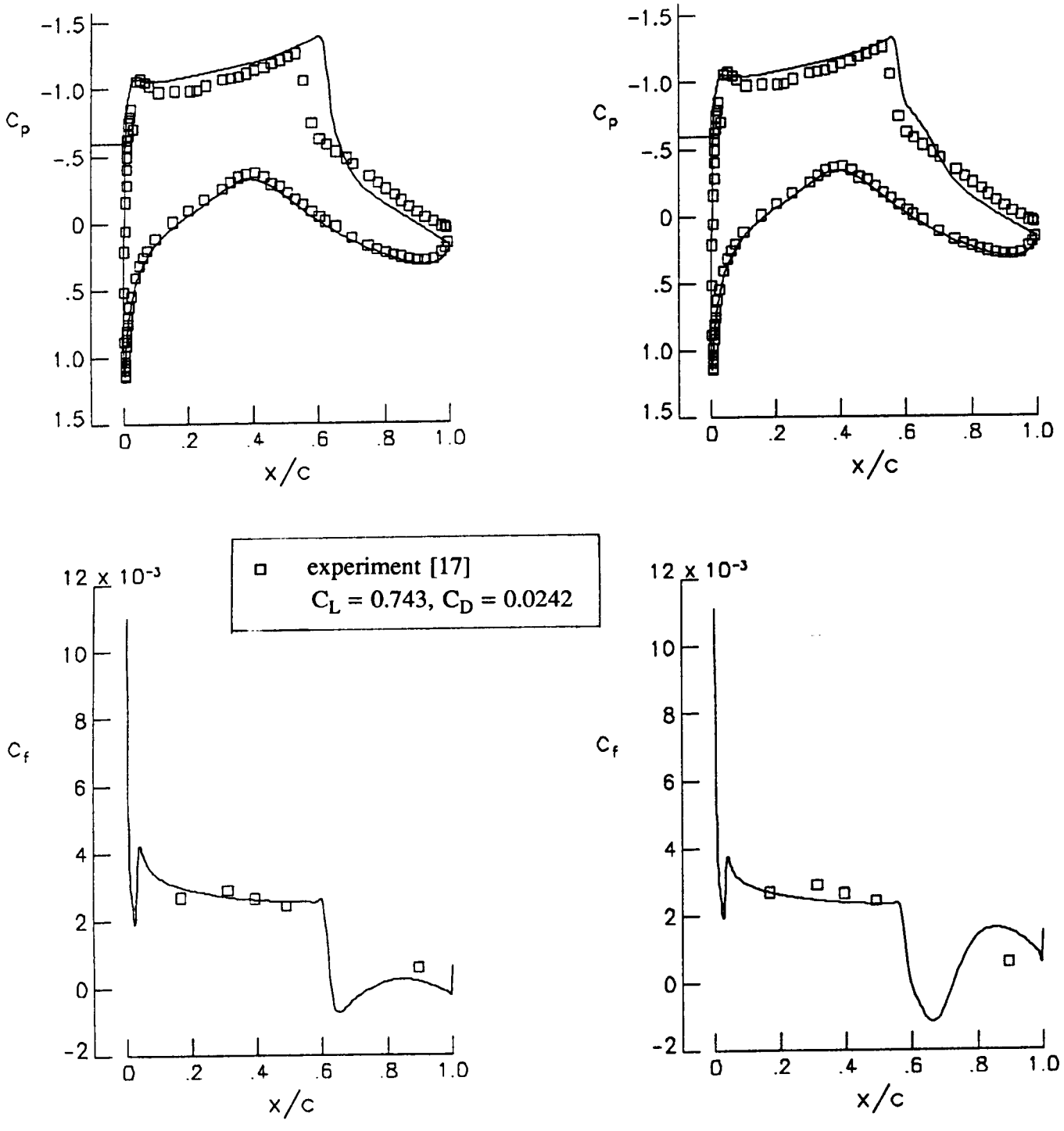

a) B.-L. model
C_L = 0.851, C_D = 0.0289

b) J.-K.-mod. model
C_L = 0.810, C_D = 0.0264

Fig. 10 : Effect of the turbulence model on distributions of pressure and skin friction for RAE 2822 airfoil (M_∞=0.75, α=2.81°, Re_∞=6.5x10^6, grid 481x97).

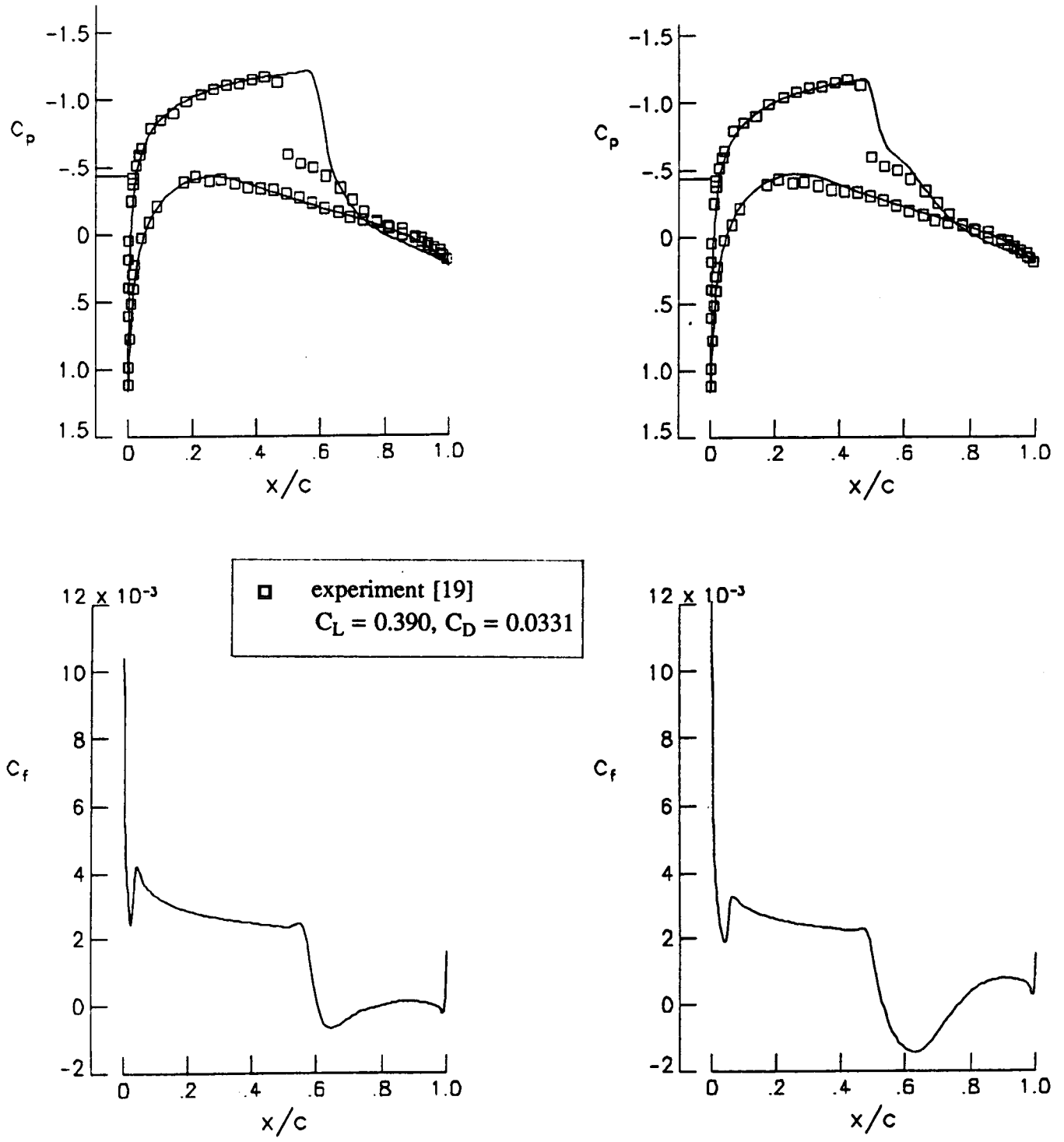

a) B.-L. model
C_L = 0.466, C_D = 0.0434

b) J.-K.-mod. model
C_L = 0.386, C_D = 0.0378

Fig. 11 : Effect of the turbulence model on distributions of pressure and skin friction for NACA 0012 airfoil (M_∞=0.799, α=2.26°, Re_∞=9.0x10^6, grid 321x65).

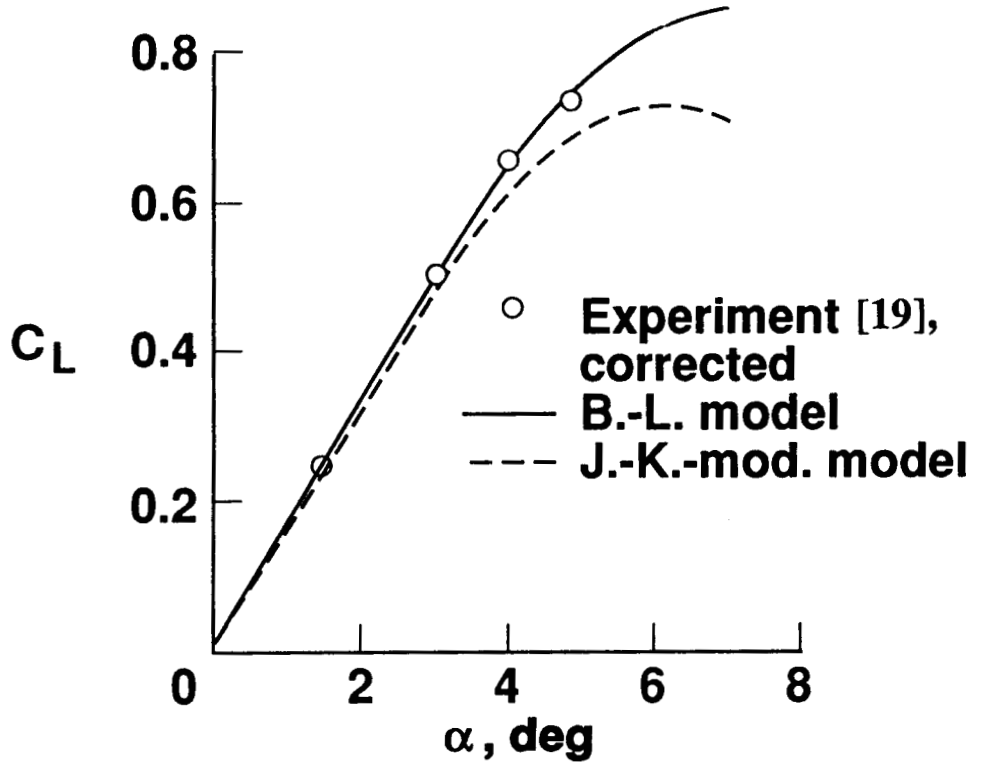

Fig. 12 : Comparison of lift coefficient versus angle of attack for the NACA 0012 airfoil, M_∞=0.7, Re_∞=9.0x10^6, grid 321x65.

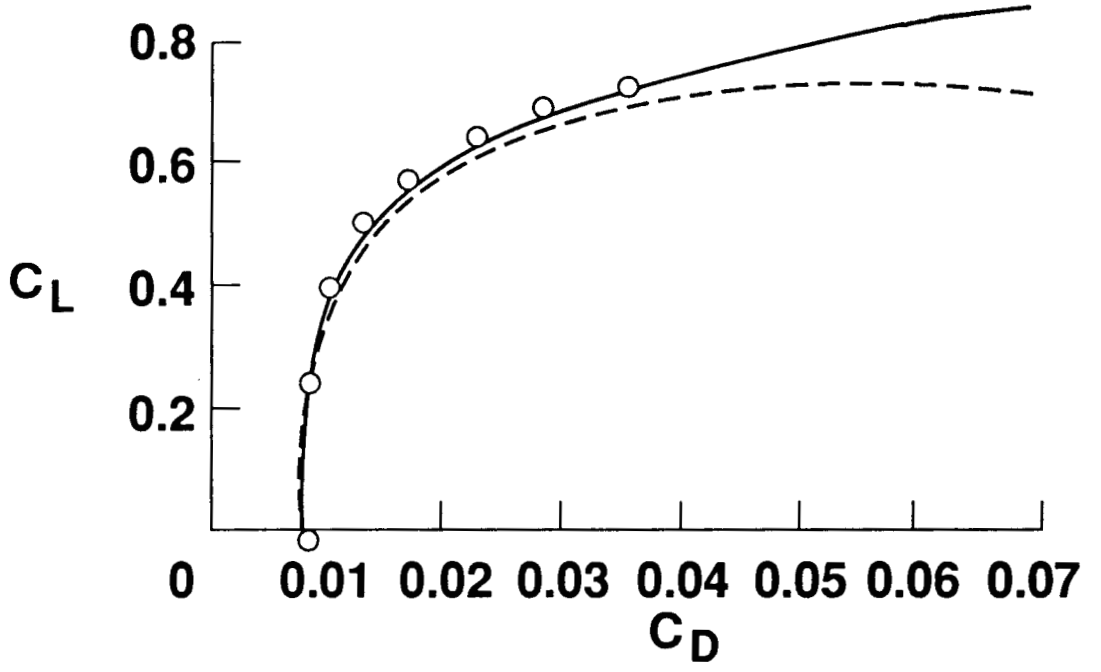

Fig. 13 : Comparison of lift versus drag polars for the NACA 0012 airfoil, M_∞=0.7, Re_∞=9.0x10^6, grid 321x65.

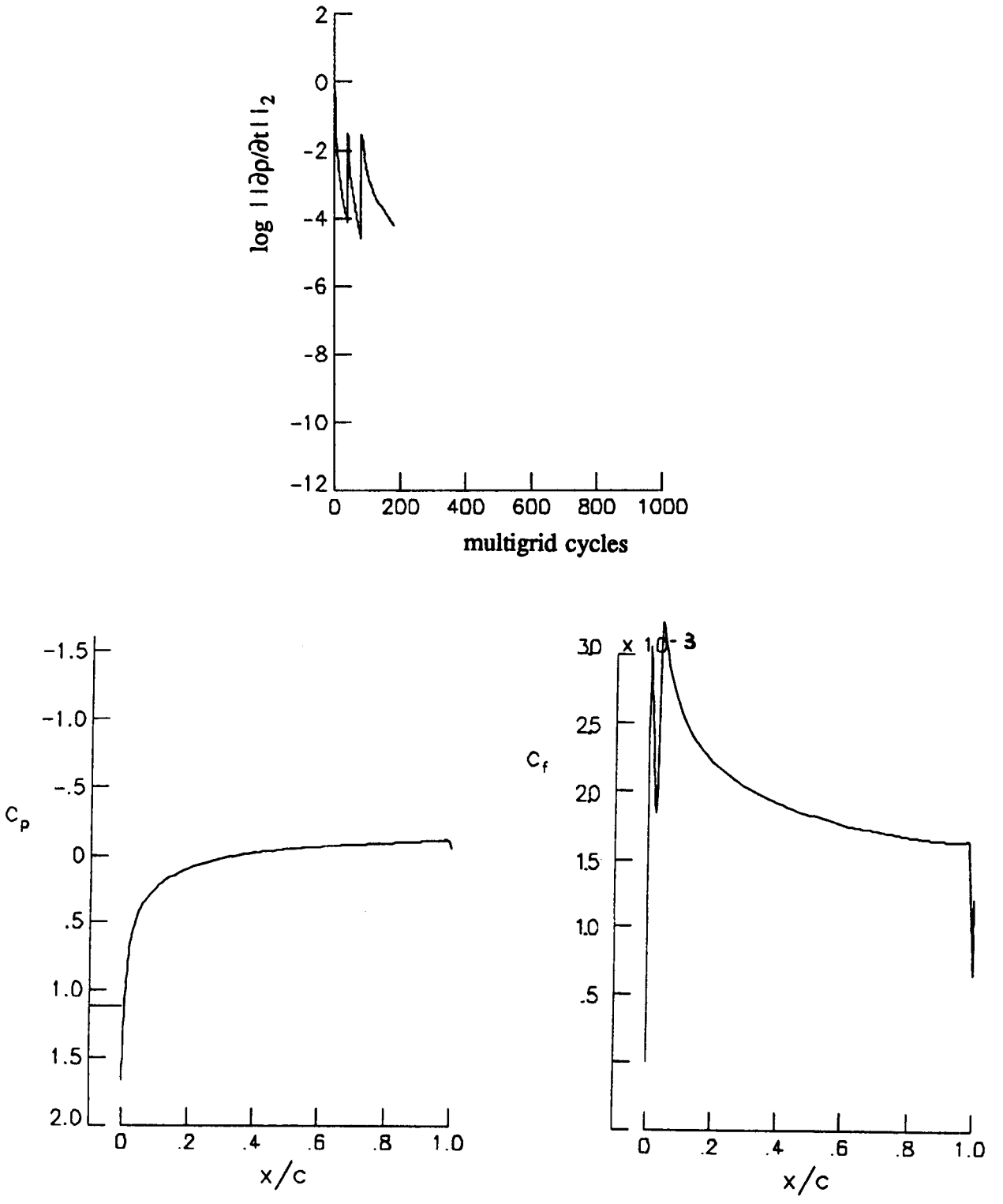

Fig. 14 : Convergence history and distributions of pressure and skin friction for turbulent supersonic flow around NACA 0012 airfoil, M_∞=2.0, α=0°, Re_∞=10.0x10^6, grid 321x65, computed with the B.-L. model.

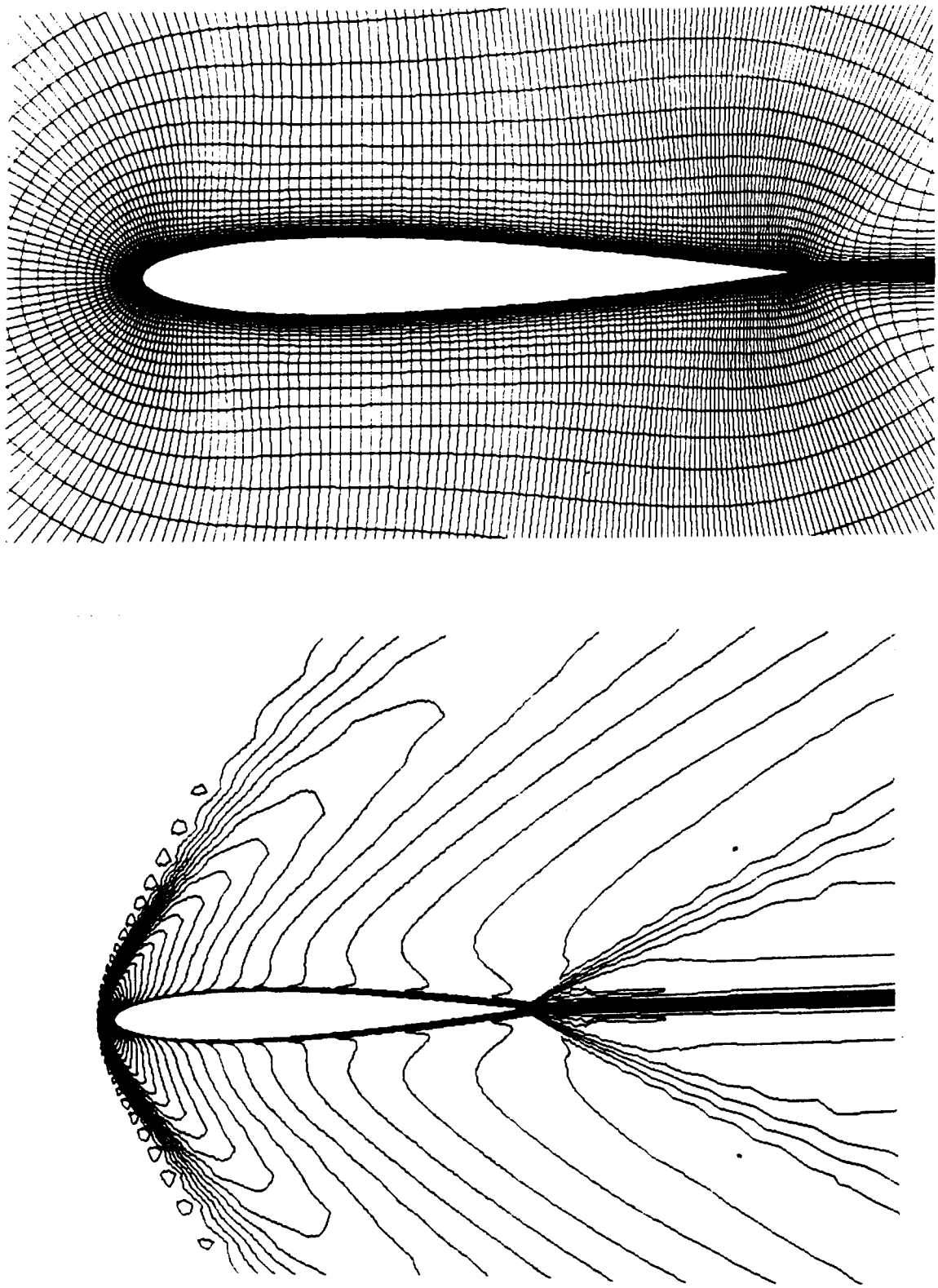

Fig. 15 : Mach contours and 321x65 mesh for turbulent supersonic flow around NACA 0012 airfoil, M_∞=2.0, α=0°, Re_∞=10.0x10^6, computed with the B.-L. model.

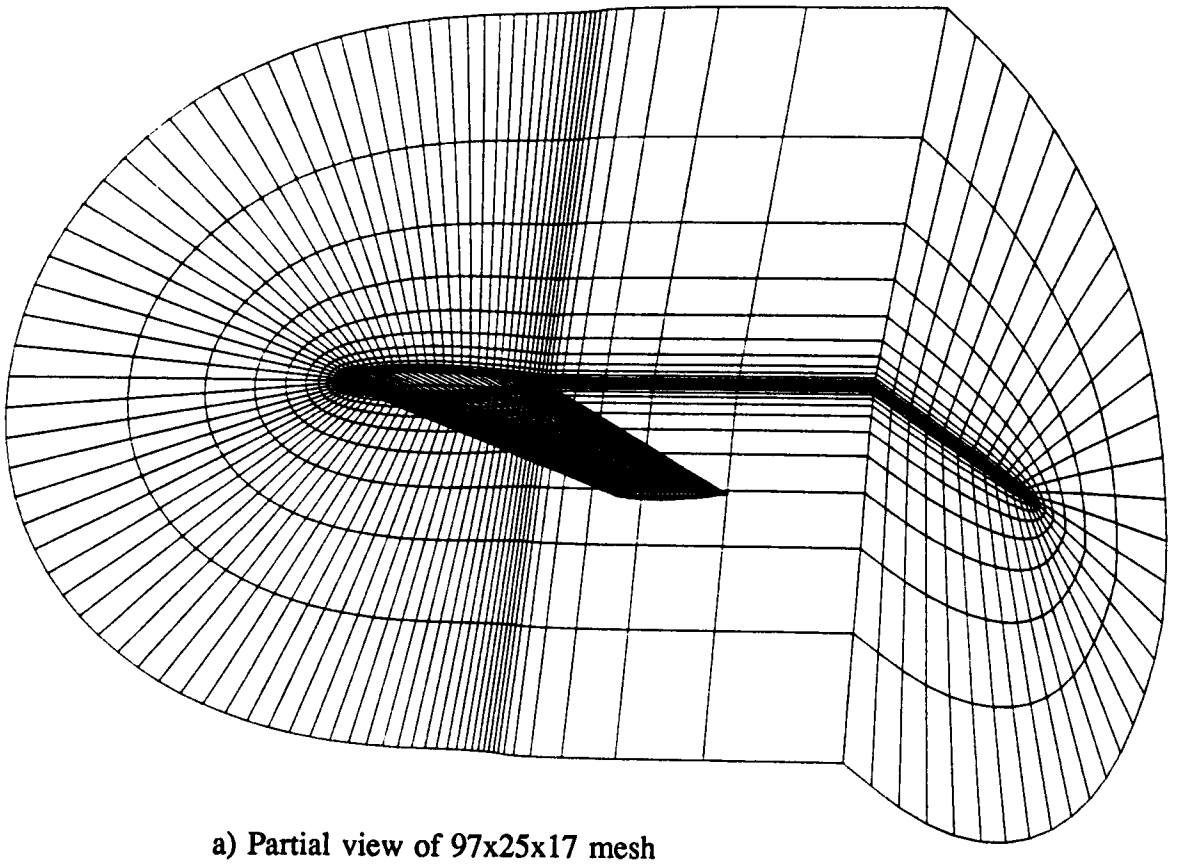

a) Partial view of 97x25x17 mesh

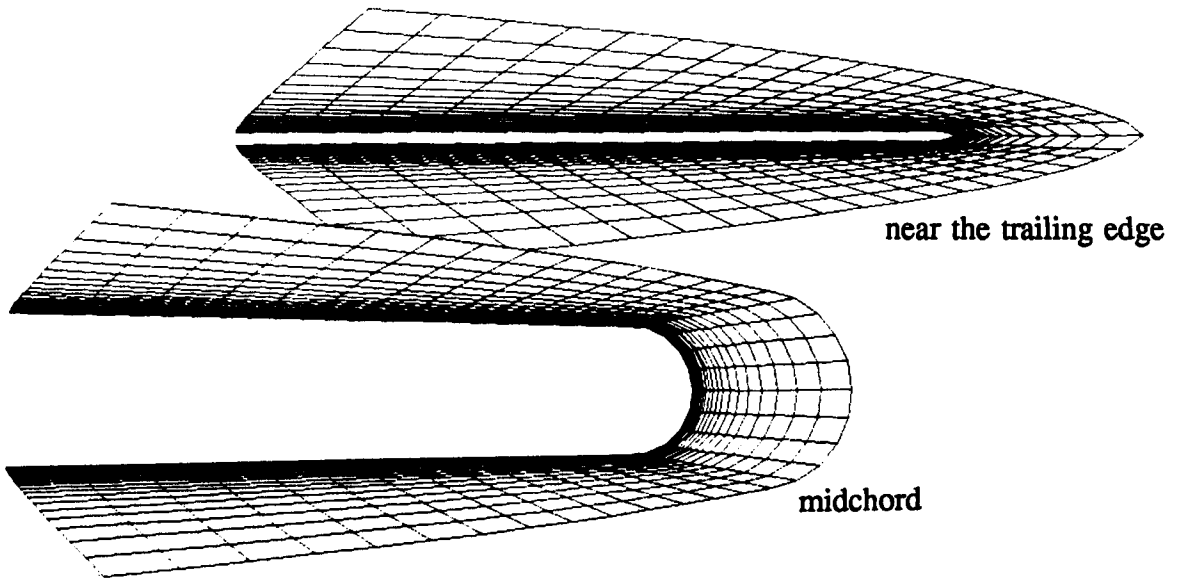

b) Spanwise sections of 289x65x49 mesh at the wing tip

Fig. 16 : Coordinate grid around ONERA-M6 wing.

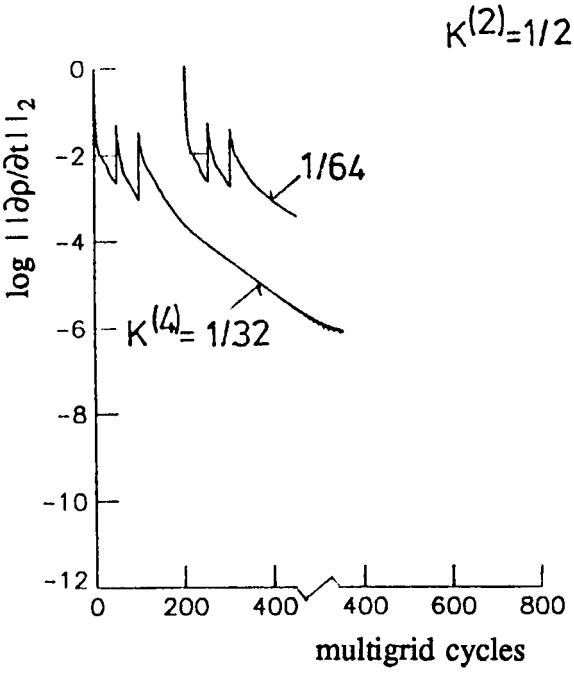

a) Influence of fourth-difference dissipation on convergence, single time step on coarse meshes, α=3.06°, B.-L. model

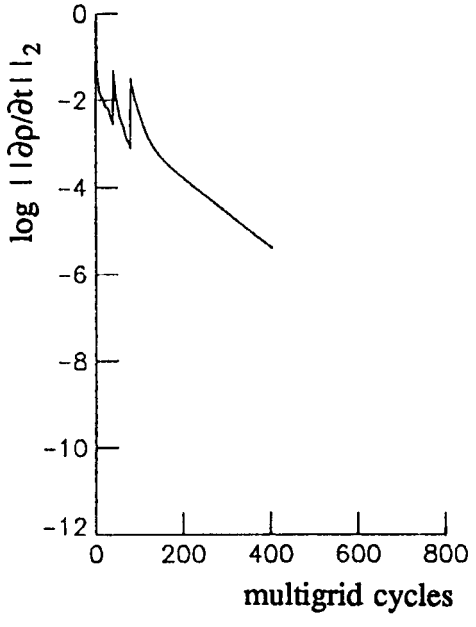

b) Convergence for two time steps on coarse meshes, $K^{(4)}$=1/32, α=3.06°, B.-L. model.

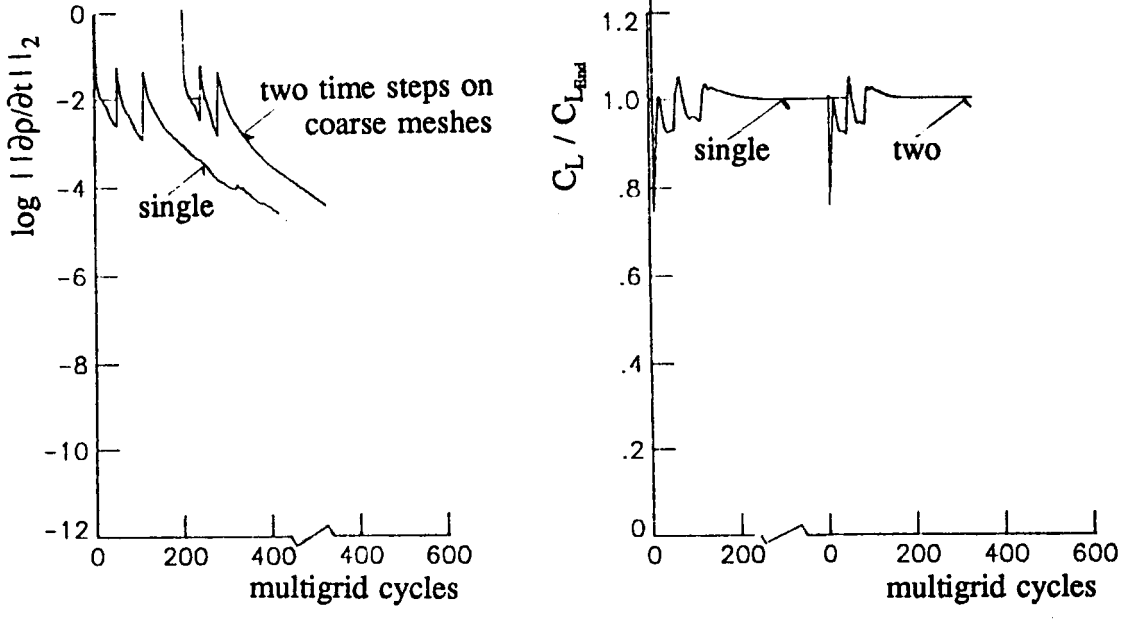

c) Convergence for nonequilibrium J.-K.-mod. turbulence model, $K^{(4)}$=1/32, α=6.06°.

Fig. 17 : Convergence behavior for transonic flow around ONERA-M6 wing M_∞=0.84, Re_∞=11.0x10^6, mesh 289x65x49

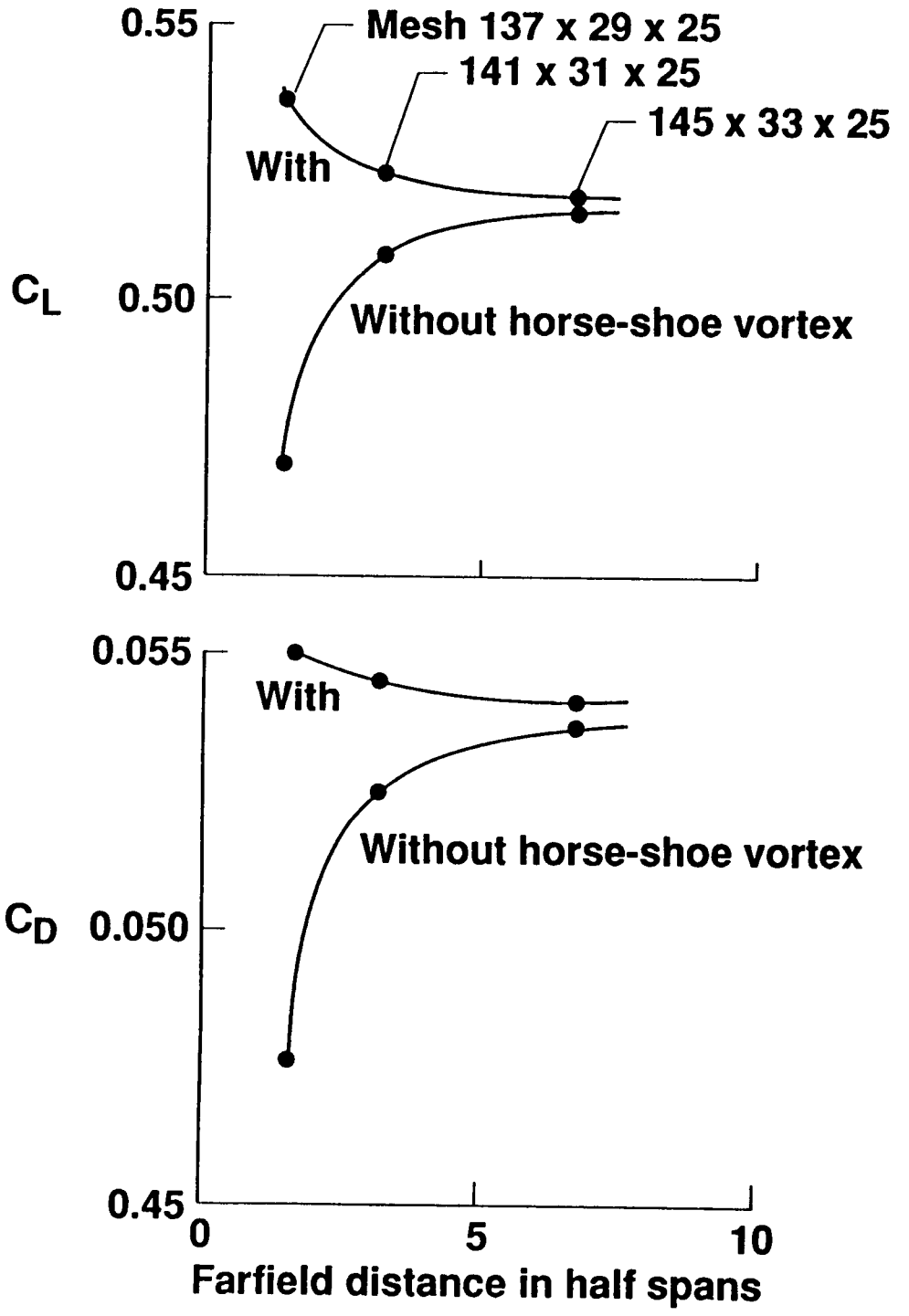

Fig. 18 : Lift and drag coefficients versus distance to the far-field boundary for transonic flow over ONERA-M6 wing M_∞=0.84, α = 6.06°, Re_∞=11.0x10^6.

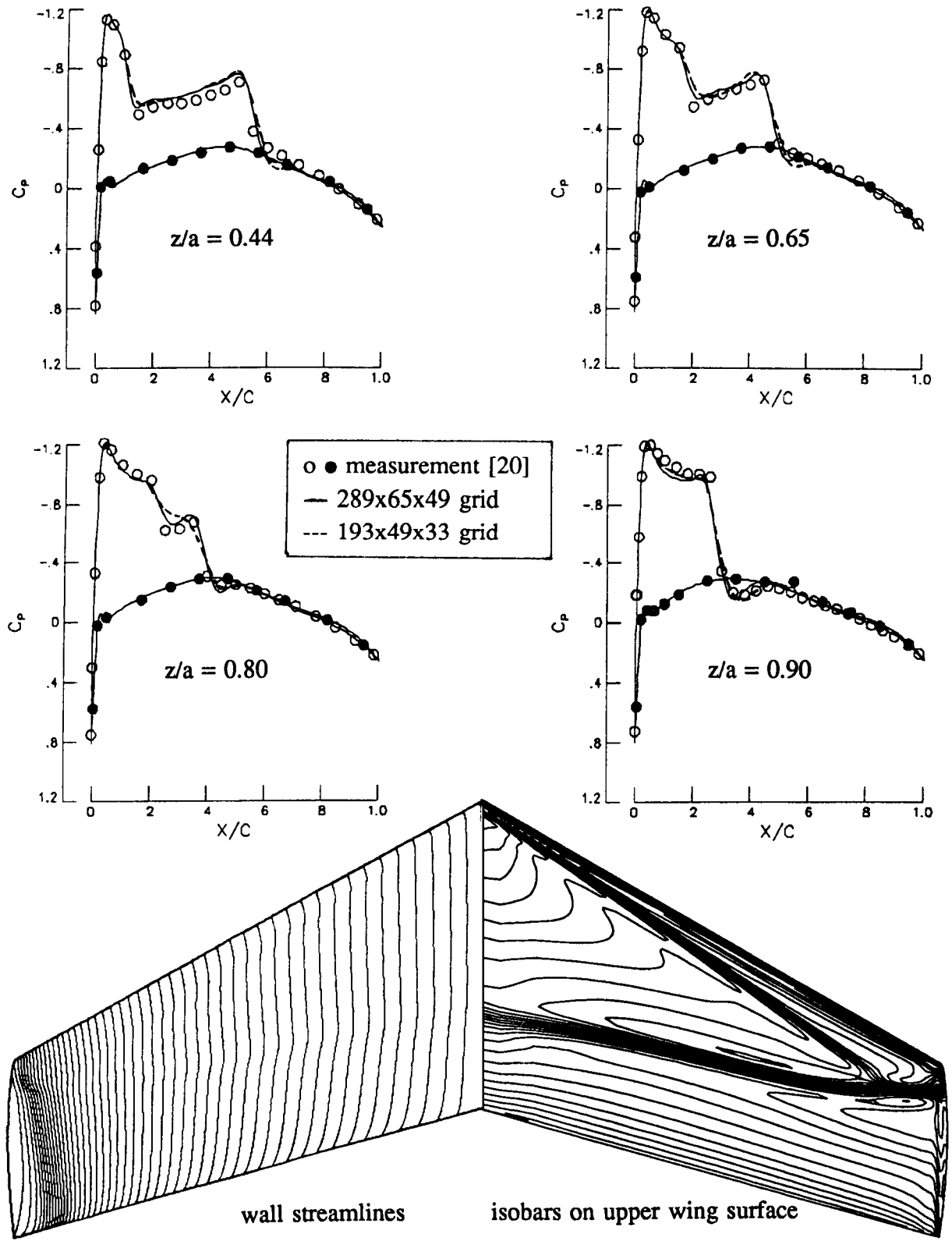

Fig. 19 : Pressure distributions and wall streamlines for ONERA-M6 wing, M_∞=0.84, α = 3.06°, Re_∞=11.0x10^6, $K^{(4)}$=1/32, computed with the B.-L. model.

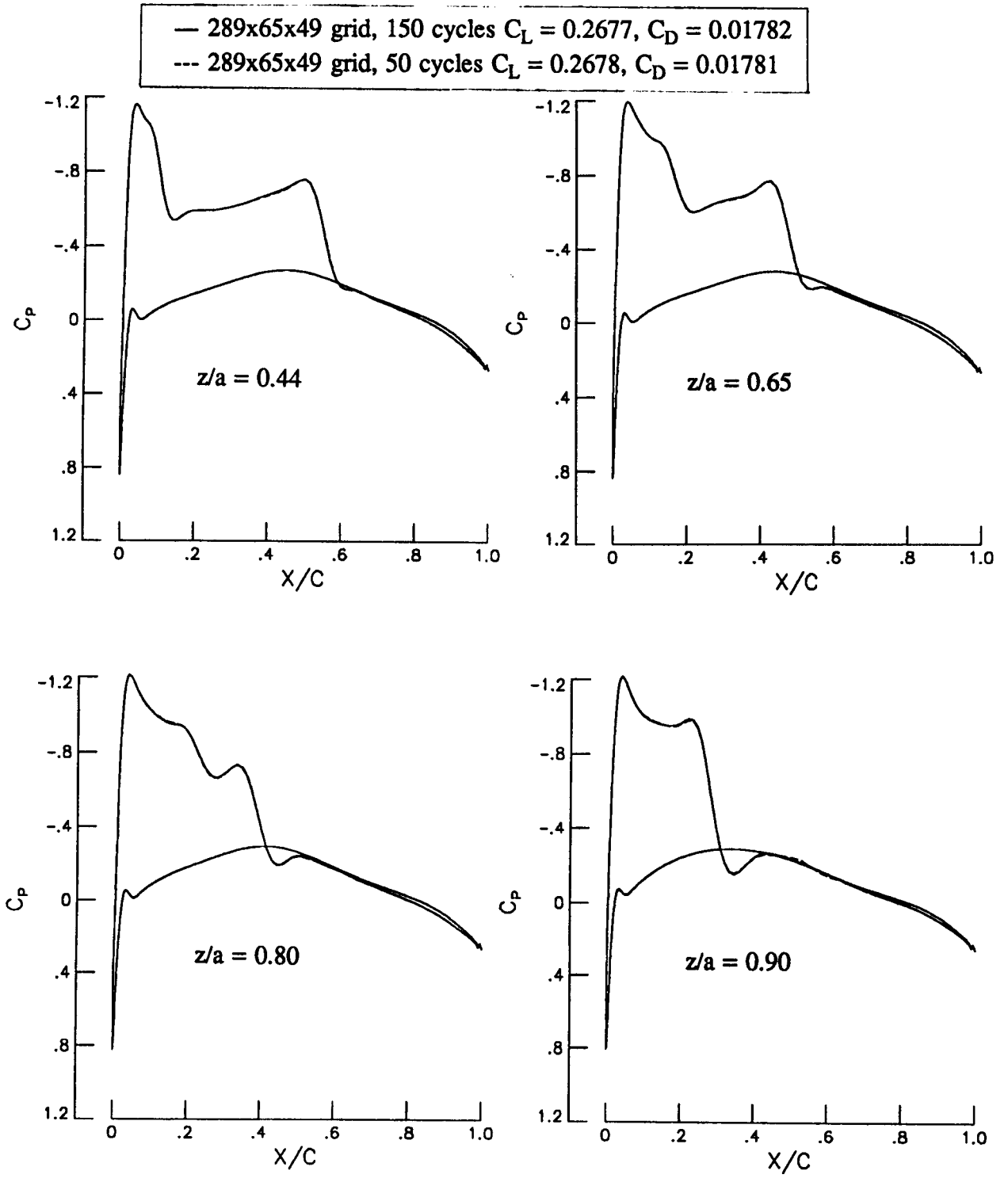

Fig. 20 : Comparison of pressure distributions on ONERA-M6 wing, M_∞=0.84, $\alpha = 3.06^o$, Re_∞=11.0x10^6, $K^{(4)}$=1/32, B.-L. model, after 50 multigrid cycles with the fully converged result, two time steps on the coarse meshes.

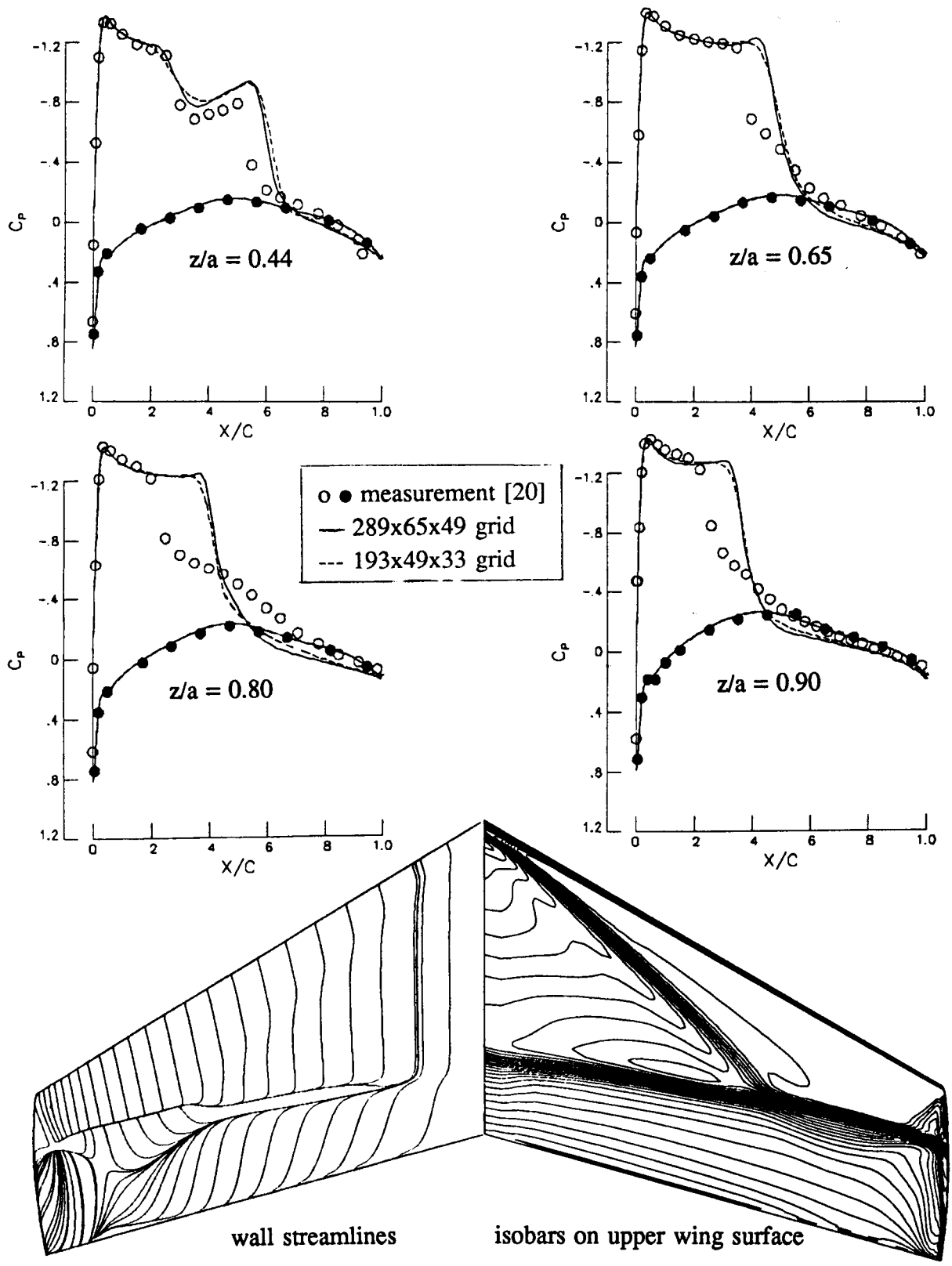

Fig. 21 : Pressure distributions and wall streamlines for ONERA-M6 wing, M_∞=0.84, α = 6.06°, Re_∞=11.0x10^6, $K^{(4)}$=1/32, computed with the B.-L. model.

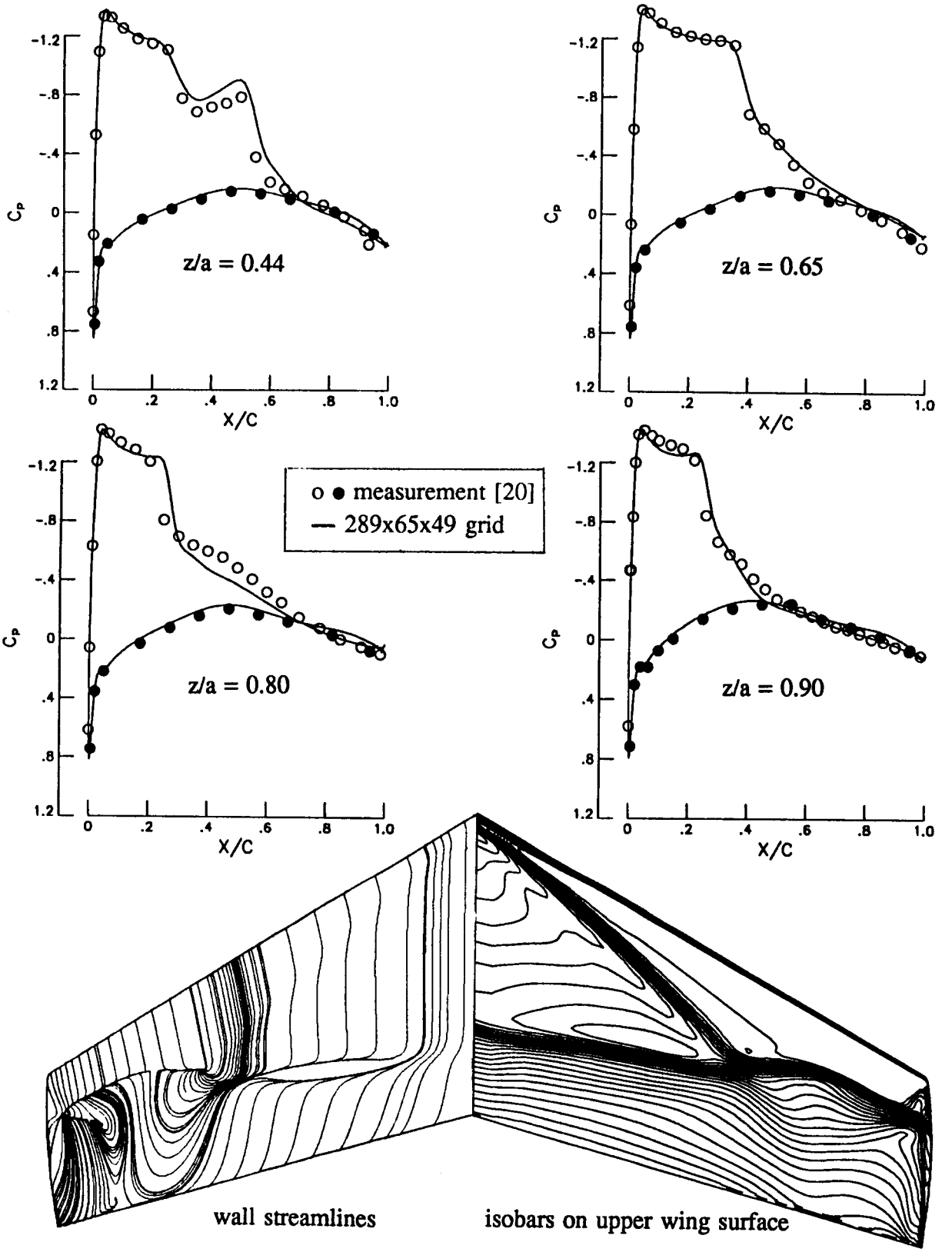

Fig. 22 : Pressure distributions and wall streamlines for ONERA-M6 wing, M_∞=0.84, α = 6.06°, Re_∞=11.0x10^6, $K^{(4)}$=1/32, computed with the J.-K.-mod. model.

NASA National Aeronautics and Space Administration

Report Documentation Page

1. Report No.	2. Government Accession No.	3. Recipient's Catalog No.
NASA TM-101557		

4. Title and Subtitle	5. Report Date
A Cell-Vertex Multigrid Method for the Navier-Stokes Equations	January 1989
	6. Performing Organization Code

7. Author(s)	8. Performing Organization Report No.
R. Radespiel	
	10. Work Unit No.
	505-60-01-01

9. Performing Organization Name and Address	11. Contract or Grant No.
NASA Langley Research Center Hampton, VA 23665-5225	
	13. Type of Report and Period Covered
12. Sponsoring Agency Name and Address	Technical Memorandum
National Aeronautics and Space Administration Washington, DC 20546-0001	14. Sponsoring Agency Code

15. Supplementary Notes

R. Radespiel: NASA-NRC Resident Research Associate at Langley, now at the Institute for Design Aerodynamics, DFVLR, Göttingen, West Germany (FRG).

16. Abstract

A cell-vertex scheme for the Navier-Stokes equations, which is based on central difference approximations and Runge-Kutta time stepping, is described. Using local time stepping, implicit residual smoothing, a multigrid method, and carefully controlled artificial dissipative terms, very good convergence rates are obtained for a wide range of two- and three-dimensional flows over airfoils and wings. The accuracy of the code is examined by grid refinement studies and comparison with experimental data. For an accurate prediction of turbulent flows with strong separations, a modified version of the nonequilibrium turbulence model of Johnson and King is introduced, which is well suited for an implementation into three-dimensional Navier-Stokes codes. It is shown that the solutions for three-dimensional flows with strong separations can be dramatically improved, when a nonequilibrium model of turbulence is used.

17. Key Words (Suggested by Author(s))	18. Distribution Statement
Navier-Stokes Equations Numerical Methods	Unclassified-Unlimited Subject Category 02

19. Security Classif. (of this report)	20. Security Classif. (of this page)	21. No. of pages	22. Price
Unclassified	Unclassified	40	A03